Carnegie-Mellon University
PITTSBURGH, PENNSYLVANIA 15213

DEPARTMENT OF
MECHANICAL ENGINEERING

A STUDY OF FRACTURE PHENOMENA IN FIBER COMPOSITE LAMINATES

H. J. Konish, Jr.

Report SM-73-13

April 1973

This work was supported by

Air Force Contracts F33615-70-C-1146 and F33615-72-C-1214

and NASA Research Grant NGR-39-002-023

Department of Mechanical Engineering

Carnegie Institute of Technology

Carnegie-Mellon University

Pittsburgh, Pennsylvania

A STUDY OF FRACTURE PHENOMENA IN FIBER COMPOSITE LAMINATES

H. J. Konish, Jr.

Report SM-73-13 April 1973

Submitted in partial fulfillment of the
requirements for the degree of
Doctor of Philosophy at Carnegie-Mellon University

Department of Mechanical Engineering
Carnegie Institute of Technology
Carnegie-Mellon University
Pittsburgh, Pennsylvania

ABSTRACT

The extension of linear elastic fracture mechanics from ostensibly homogeneous isotropic metallic alloys to heterogeneous anisotropic advanced fiber composites is considered. It is analytically demonstrated that the effects of material anisotropy do not alter the principal characteristics exhibited by a crack in an isotropic material. The heterogeneity of fiber composites is experimentally shown to have a negligible effect on the behavior of a sufficiently long crack.

A method is proposed for predicting the fracture strengths of a large class of composite laminates; the values predicted by this method show good agreement with limited experimental data. The limits imposed by material heterogeneity are briefly discussed, and areas for further study are recommended.

ACKNOWLEDGMENTS

The author is pleased to acknowledge the guidance and encouragement of Dr. T. A. Cruse throughout the course of this work. This endeavor has also been strongly influenced by Dr. J. L. Swedlow, to whom the author is likewise indebted.

The support of this work by the United States Air Force, under Contracts F33615-70-C-1146 and F33615-72-C-1214, and the National Aeronautics and Space Administration, under Research Grant NGR-39-002-023, is gratefully acknowledged. The author also wishes to express his thanks to the Convair Aerospace Division of General Dynamics Corporation, which furnished the specimens for the experimental part of this work. The generous personal support of the Fannie and John Hertz Foundation is deeply appreciated.

Finally, the author's special gratitude is extended to Ms. K. J. Sokol, for her patient and diligent preparation of this typescript.

TABLE OF CONTENTS

FIGURES

TABLES

LIST OF SYMBOLS

α	Fiber orientation angle.
β_{ij}	Components of compliance matrix for a two-dimensionally anisotropic material; i,j = 1,2,6.
δ	Incremental amount of collinear crack growth.
$\varepsilon_x, \varepsilon_y, \gamma_{xy}$	Global engineering strain components.
Γ	Integration path around the crack tip.
λ_k	Constant of integration; k = 1,2.
k_i	Relative thickness of the i^{th} angle-ply component of a specially orthotropic laminate.
μ_k	Characteristic material parameters of a two-dimensionally anisotropic material; k=1,2.
υ	Poisson's ratio for an isotropic material.
υ_{12}	Principal Poisson's ratio for a fiber composite ply.
ϕ	Orientation angle of applied tensile stress, relative to the crack.
ϕ_i	Ply orientation angle of the i^{th} angle-ply component of a specially orthotropic laminate.
$\Phi_k\ (z_k)$	Complex stress functions; k = 1,2.
$\sigma_x, \sigma_y, \tau_{xy}, \sigma_{ij}$	Global stress components; i, j= 1, 2.

σ_1, σ_2	Stress component relative to the material coordinate system of a given ply.
σ_{1u}, σ_{2u}	Principle tensile strengths of a fiber composite ply.
σ_o	Applied remote tensile stress.
τ_o	Applied remote shear stress.
θ	Elliptical or polar angular coordinate.
$\{\xi_j\}_i$	Vector portion of stress expression in the ith ply of a specially orthotropic laminate; j = 1,2,3.
ζ_k	Mapped complex coordinates; k = 1,2.
$e^{i\theta}$	Complex representation of a unit circle.
$f^{\xi}_{ij}, g^{\xi}_{i}, h^{\xi}_{ij}, k^{\xi}_{i}$	Spatial distribution functions; i,j=1,2; ξ=I,II.
(r,θ)	Polar coordinates.
a	Half-length of crack; semi-major axis of ellipse.
a_m, b_m, c_m, d_m	Complex Fourier coefficients.
A_k	Magnitude of net applied load on an internal boundary.
A_{km}	Complex coefficients of Laurent series expansion.
b	Semi-minor axis of ellipse.
B	Thickness of three-point bend specimen.
E	Tensile modulus of isotropic material.
E_{11}	Major tensile modulus of fiber composite ply.

E_{22}	Transverse tensile modulus of fiber composite ply.
G	Shear modulus of isotropic material.
G_{12}	Principal shear modulus of fiber composite ply.
$\mathcal{G}$	Strain energy release rate.
$\mathcal{G}_Q$	Value of the strain energy release rate corresponding to initial crack instability.
Im	Imaginary part of a complex number.
J	Rice's J-integral.
J_Q	Value of Rice's J-integral corresponding to initial crack instability.
K_ξ	Stress intensity factor; ξ= I, II.
$K_{\xi Q}$	Fracture strength, i.e., the value of the stress intensity factor at initial crack instability.
$\overline{K}_Q$	Average fracture strength of several specimens.
K_{If}	Predicted value of fracture strength corresponding to crack growth across fibers.
K_{Im}	Predicted value of fracture strength corresponding to crack growth between fibers.
ℓ_o	Estimated size of crack-tip region.
L	Length of center-cracked tensile specimen.
ℓn	Natural logarithm.
log	Common logarithm.
M_o	Slope of initial linear portion of load-displacement curve.

$O[\ ]$	Increasing power series beginning with the term in the brackets.
P	Load applied to three-point bend specimen.
P_k, q_k	Displacement coefficients; $k = 1,2$.
$[\bar{Q}_{mn}]_i$	Global stiffness matrix of the ith ply of a laminate; $m, n = 1, 2, 6$.
r_f, r_m	Characteristic sizes of damage zones surrounding the crack tip.
Re	Real part of a complex number
ds	Increment of integration path Γ.
S	Span of three-point bend specimen.
t_r, t_θ	Components of traction vector on elliptical boundary.
$\underset{\sim}{T}$	Traction vector on integration path Γ.
T_x, T_y	Cartesian components of traction vector.
$[T_{mn}]_i$	Stress rotation matrix for the ith ply of a laminate.
u, v, u_i	In-plane components of displacement; $i = 1,2$.
$\underset{\sim}{u}$	Displacement vector on integration path Γ.
w	Strain energy density.
W	Width of center-cracked tension specimen; depth of three-point bend specimen.
(x, y)	Cartesian coordinates.
Y	Finite correction factor.
z_k	Characteristic complex coordinates in a two-dimensionally anisotropic material; $k=1, 2$.

CHAPTER I

INTRODUCTION

I.1 Rationale

The failure of many metallic structures is attributed to the fact that, under cyclic loading, a sharp crack may form at the site of a stress concentration, which may be inherent to either the material (e.g., a brittle inclusion) or the structure (e.g., a fastener hole). The nature of the site of crack formation is a secondary question, however, once the sharp crack has been developed, for that crack grows incrementally under further cyclic loading until it attains some critical size. Subsequent application of load causes abrupt, unstable growth of this critical crack, and thus, complete failure of the structure. The abrupt nature of this failure mode, in combination with the often undetectable growth of the crack to critical size, is responsible for the widespread interest in fracture of metals.

At first glance, the problem of fracture does not appear to be as critical in advanced fiber composites as in metals, since cyclic loading does not induce sharp cracks in fiber composite structures. A study of fracture in advanced fiber composites is nevertheless of interest for a number of reasons, the most obvious of which is that cyclic loading is not the sole cause of sharp notches in a structure. Sharp, crack-like flaws may be present in a fiber composite structure for any number of reasons, ranging from improper fabrication of the

material to in-service damage of the structure. An investigation of such defects in fiber composites is clearly warranted by the critical nature of sharp flaws in metals.

A second reason for the study of fracture in fiber composites is the behavior of certain types of blunt notches in such materials. For example, it has been shown that the tensile strength of a composite laminate containing a small circular notch is dependent upon the size of that notch [1,2]. This phenomenon, which cannot be explained by the stress concentration model used in metals, has been successfully modelled as a fracture problem [3]. Furthermore, the fracture approach suggested in [3], though presently somewhat tentative, is not restricted to any single notch geometry, and may be applicable to the analysis of any blunt notch in a fiber composite structure.

Yet another motivation for a study of fracture in advanced fiber composites stems from the current interest in fail-safe structures. Clearly, the design of such structures requires some characterization of the damage to be contained, which is typically modelled as a running crack. The successful application of a fracture approach to the design of fail-safe composite panels has recently been demonstrated [4].

The study of fracture in fiber composites is also justified by a very pragmatic consideration, namely that composite materials compete directly with metallic alloys. Naturally, the choice between these

two types of materials must be based, in part, on the form and degree of notch sensitivity exhibited by each. Thus, the effects of sharp notches in fiber composites must be evaluated, in order to provide additional data for an objective choice between composites and metals.

As noted above, cyclic loading of fiber composites does not create sharp cracks, as it does in metals. A study of fracture in fiber composites is clearly warranted, however, for the purposes of material characterization and structural design. It is in recognition of these needs that the work reported herein was performed.

I.2 Background and perspective

Fracture in fiber composite materials may be considered from two distinct points of view, both of which are well represented in the literature. Ths primary difference between these two approaches is one of scale, from which distinction it follows that certain advantages and disadvantages are associated with each approach. It is emphasized that these two approaches must be viewed as complementary, and not mutually exclusive.

The micromechanics approach to composite fracture [5-7] is based, as the name implies, on a detailed model of a fiber composite material. This model consists of a single unidirectional layer of parallel discrete fibers, embedded in a matrix material, and subjected to a tensile load in the fiber direction. This layer contains a single crack, aligned

in the transverse fiber direction; the crack itself, and the stress field which it induces, are characterized in terms of numbers of fibers. The simplicity of this material model permits the effects of parameters such as fiber-matrix bond strength and constituent material properties on crack growth to be evaluated [8-10]. Such information is of significant value to the material supplier, as it indicates ways of improving the fracture resistance of the basic material. To the structural designer, however, the micromechanics approach is of little use, for real composite structures always contain many layers of fibers, and are often multi-directional as well. The characterization of fracture in fiber composites under these more complex conditions clearly requires a more general approach than that provided by micromechanics.

A means of characterizing fracture in a structural composite laminate is suggested by studies of fracture in metals, which are typically performed within the framework of linear elastic fracture mechanics (LEFM). The application of metals-based LEFM to fiber composite laminates is predicated on a material model which differs markedly from that used in the micromechanics approach, in that the composite laminate is assumed to be homogeneous. The heterogeneity of the real material is considered only as a limit to the validity of the homogeneous model. The LEFM approach thus lacks some of the rigor of the micromechanics approach. However, it is not as restricted as the micromechanics approach either; in particular, multi-directional

laminates present no difficulty with the LEFM approach. Moreover, the severity of a sharp notch is not characterized in terms of a number of broken fibers, but in terms of the structural parameters of crack length and applied load.

Metals-based LEFM was first applied to the study of fiber composites for the particularly simple case of a unidirectional material containing a crack parallel to the fiber direction [11-12]. In view of the problem considered, it is not surprising that LEFM was found to characterize the conditions under which crack growth occurred. The extension of LEFM to the study of crack growth in more general composite laminates is really quite recent, a prime example being this work, though reports of other similar investigations are now beginning to appear [13-15].

I.3 Scope of the study

An investigation of fracture in advanced fiber composites, using the concepts and procedures of metals-based LEFM, is discussed in this report. In the first part of the report (chapters II and III), the analytical investigation of the stress field induced by a sharp crack in an anisotropic homogeneous material is described. The comparison of these results to those obtained for a similar study in isotropic materials indicates that anisotropy has no effect on the form of the crack-induced stress field, and very little effect on its magnitude. Thus, the anisotropy of fiber composite laminates presents no obstacle

to the use of metals-based LEFM. In chapters IV and V, the results of an experimental program are described. It is shown that the test data, when reduced according to the procedures specified for metals-based LEFM, appear to characterize the initiation of crack growth in the test specimens. This result suggests that, at least for the conditions of the test program, the heterogeneity of fiber composites is largely negligible. In chapter VI, a method is proposed for predicting the conditions under which unstable crack growth will occur in a fiber composite laminate. Also contained in chapter VI is a discussion of the guidelines for using a homogeneous material model as the basis for characterizing fracture in advanced fiber composites.

CHAPTER II

STRESS ANALYSIS OF A CRACK IN THE ANISOTROPIC PLANE

II.1 Introduction

Fundamental to the characterization of cracks in structural members is an investigation of the stress and displacement fields near the tip of a sharp crack. In particular, the nature of the stress singularity at the crack tip must be determined. Of equal significance is the manner in which the magnitudes of the stress and displacement fields near the crack tip are related to structural geometry and loading. These topics have been thoroughly investigated in isotropic materials, and much of metals-based LEFM is predicated upon the results of such investigations.

It follows that a study of the stress and displacement fields in the crack-tip region of an anisotropic material is of basic importance to any application of metals-based LEFM to anisotropic materials, such as fiber composite laminates. One such study is presented below.

II.2 Formulation of the problem

The problem to be considered in this section is that of an unbounded plane, containing a single one-dimensional crack of length $2\mathring{a}$, located along the x-axis (Figure 1). The plane is subjected to remote loading consisting of a uniaxial in-plane tensile stress σ_o, and an in-plane shear stress τ_o. The arbitrary orientation of the tensile stress within the plane of the problem is denoted by the angle ϕ.

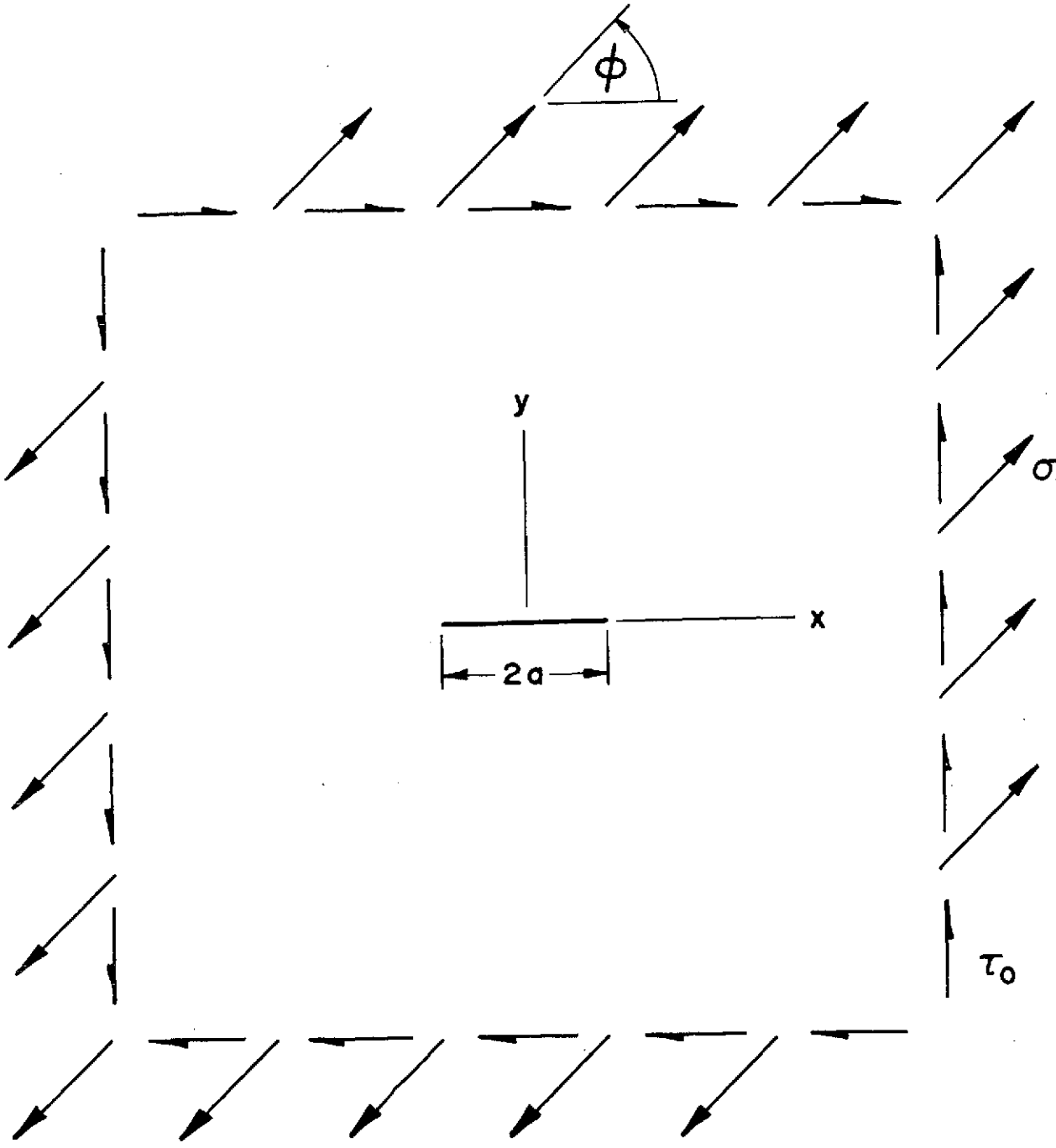

Figure 1. One-dimensional crack in the infinite plane, under mixed, in-plane, remote loading.

The constitutive relationship used for this problem represents a homogeneous, linear elastic, anisotropic material. The anisotropy is confined to the plane of the problem, and is further restricted by the requirement that any out-of-plane displacements be independent of x and y, the in-plane coordinates. This constitutive relation corresponds to the lamination theory representation of a mid-plane symmetric fiber composite laminate [16].

The problem of interest, as formulated above, may be solved as either a plane stress or plane strain problem, using the theory of anisotropic elasticity.

II.3 Solution technique

The solution technique for the problem of interest is the two-dimensional form of the theory of anisotropic elasticity, as presented by Lekhnitskii [17]. This formulation is much like that of two-dimensional isotropic elasticity, in that the equilibrium, strain-displacement, and compatibility relations are unaltered from their isotropic forms. The effects of anisotropy enter the problem only in the constitutive relations.

The familiar stress function approach of isotropic elasticity is used to obtain expressions for the two-dimensional stress field

$$\sigma_x = 2Re[\mu_1^2\Phi_1'(z_1) + \mu_2^2\Phi_2'(z_2)] \tag{1a}$$

$$\sigma_y = 2Re[\Phi_1'(z_1) + \Phi_2'(z_2)] \tag{1b}$$

$$\tau_{xy} = -2Re[\mu_1\Phi_1'(z_1) + \mu_2\Phi_2'(z_2)] \tag{1c}$$

where $\Phi_1(z_1)$ and $\Phi_2(z_2)$ are complex stress functions of the material dependent complex coordinates z_1 and z_2. The primes denote differentiation of the stress functions with respect to their sole arguments. These arguments (the complex coordinates) are defined by

$$z_k = x + \mu_k y \qquad k = 1, 2 \tag{2}$$

the μ_k being the complex roots of the characteristic equation of an anisotropic material. This characteristic equation has the form

$$\beta_{11}\mu^4 - 2\beta_{16}\mu^3 + (2\beta_{12}+\beta_{66})\mu^2 - 2\beta_{26}\mu + \beta_{22} = 0 \tag{3}$$

where the β_{ij} are the compliance coefficients of the material

$$\begin{Bmatrix} \varepsilon_x \\ \varepsilon_y \\ \gamma_{xy} \end{Bmatrix} = \begin{bmatrix} \beta_{11} & \beta_{12} & \beta_{16} \\ \beta_{12} & \beta_{22} & \beta_{26} \\ \beta_{16} & \beta_{26} & \beta_{66} \end{bmatrix} \begin{Bmatrix} \sigma_x \\ \sigma_y \\ \tau_{xy} \end{Bmatrix} \tag{4}$$

Expressions for the strains in terms of the stress functions may be obtained by substituting (1a-c) into (4). These strain expressions may then be integrated, using the appropriate strain-displacement and compatibility relations, to obtain expressions for the displacement field. The displacement field has the form

$$u = 2Re[p_1\Phi_1(z_1) + p_2\Phi_2(z_2)] \tag{5a}$$

$$v = 2Re[q_1\Phi_1(z_1) + q_2\Phi_2(z_2)] \tag{5b}$$

where u and v are displacement components in x- and y-directions,

respectively. The p_k and q_k, which have the forms

$$p_k = \beta_{11}\mu_k^2 - \beta_{16}\mu_k + \beta_{12} \qquad k = 1, 2 \qquad (6)$$

$$q_k = \beta_{12}\mu_k - \beta_{26} + \beta_{22}/\mu_k \qquad k = 1, 2 \qquad (7)$$

are simply convenient combinations of the compliance coefficients and the μ_k.

It is clear from (1a-c) and (5a-b) that the implementation of this solution technique is based on determining $\Phi_1(z_1)$ and $\Phi_2(z_2)$. While, in general, the stress functions are determined from boundary conditions, the details of this procedure are quite problem dependent. Thus, the topic of calculating $\Phi_1(z_1)$ and $\Phi_2(z_2)$ is deferred to an appropriate point in the solution of the specific problem of interest to this work.

II.4 The general solution

The difficulties inherent to the treatment of a perfectly sharp crack suggest the use of a somewhat circuitous approach to the actual problem of interest. Such an approach may be developed from the observation that the problem of interest may be viewed as a limiting case of a single stress-free elliptical cavity in the remotely loaded anisotropic plane (Figure 2). This problem, in turn, may be solved by the superposition of two sub-problems, the remotely loaded, featureless anisotropic plane (Figure 3a), and the internally loaded elliptical cavity in the otherwise unloaded anisotropic plane (Figure 3b).

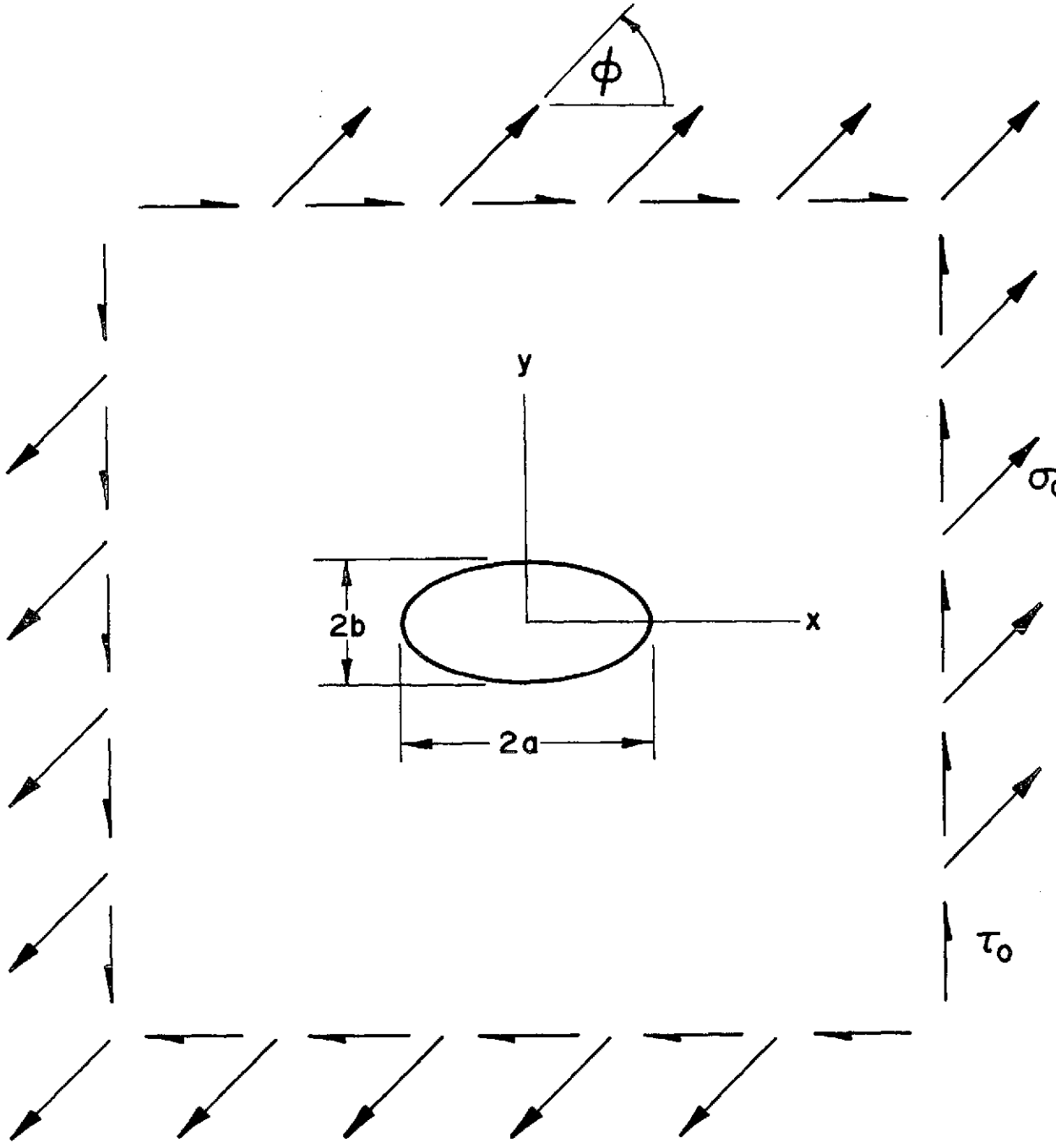

Figure 2. Stress-free elliptical cavity in the infinite plane, under mixed, in-plane, remote loading. As b approaches zero, this geometry approaches that shown in Figure 1.

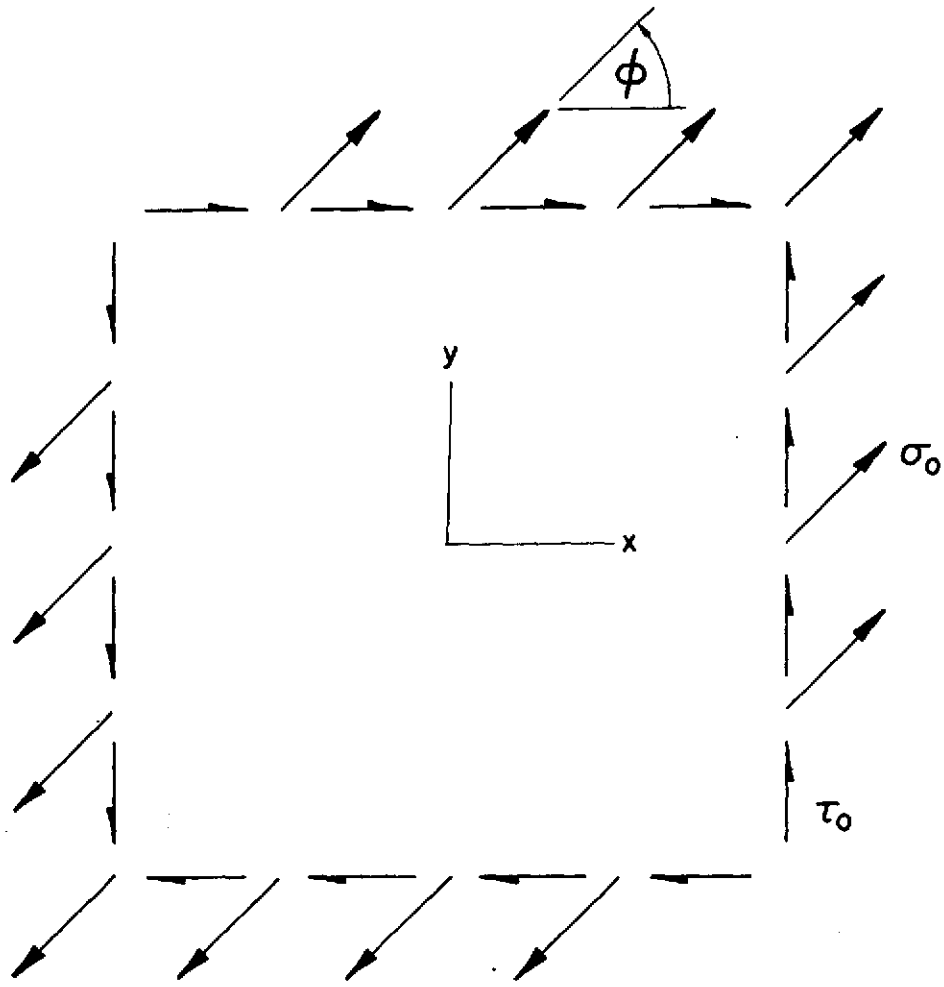

Figure 3a. Unflawed infinite plane, under mixed, in-plane, remote loading.

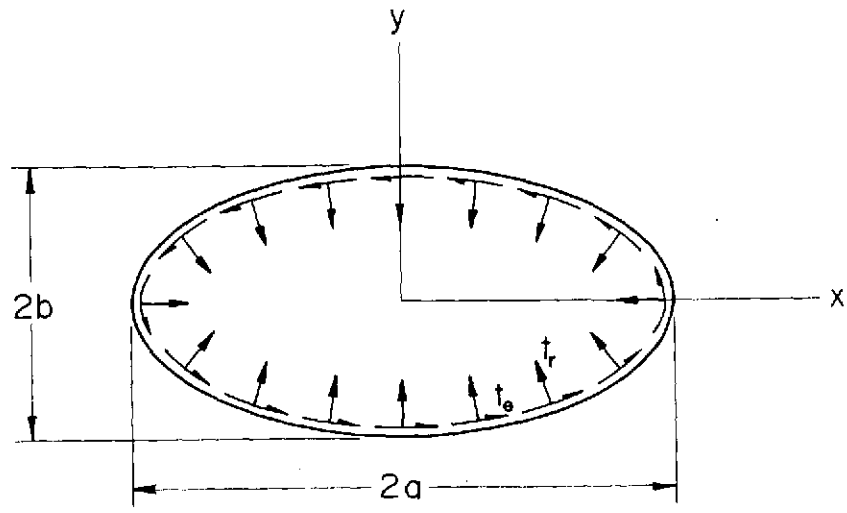

Figure 3b. Internally loaded elliptical cavity in the infinite plane, subjected to no remote loading. The tractions on the elliptical boundary, t_r and t_θ, are chosen to negate the the stress field corresponding to Figure 3a.

The solution to the first sub-problem (Figure 3a) is easily obtained without recourse to stress functions or more esoteric techniques. For this sub-problem,

$$\sigma_x^* = \sigma_o \cos^2\phi \tag{8a}$$

$$\sigma_y^* = \sigma_o \sin^2\phi \tag{8b}$$

$$\tau_{xy}^* = \tau_o + \sigma_o \sin\phi\cos\phi \tag{8c}$$

$$u^* = \sigma_x^*(\beta_{11}x+\beta_{16}y/2) + \sigma_y^*(\beta_{12}x+\beta_{26}y/2) + \tau_{xy}^*(\beta_{16}x+\beta_{66}y/2) \tag{9a}$$

$$v^* = \sigma_x^*(\beta_{12}y+\beta_{16}x/2) + \sigma_y^*(\beta_{22}y+\beta_{26}x/2) + \tau_{xy}^*(\beta_{26}y+\beta_{66}x/2) \tag{9b}$$

where the superscript asterisk denotes the solution to the first sub-problem.

The second sub-problem is more complex than the first, and its solution is correspondingly more involved. The first step in obtaining this solution is to map the physical plane of the problem (described by the complex coordinate $z = x + iy$) and the characteristic planes of the problem (described by the complex coordinates $z_k = x + \mu_k y$) onto corresponding ζ- and ζ_k-planes. This mapping is performed such that the elliptical boundaries in the z- and z_k-planes are mapped onto the unit circle in the ζ- and ζ_k-planes. Mapping functions for the elliptical boundaries are

$$\zeta = [z + \sqrt{z^2-a^2+b^2}] / (a + b) \tag{10a}$$

$$\zeta_k = [z_k + \sqrt{z_k^2-a^2-\mu_k^2 b^2}] / (a - i\mu_k b) \qquad k = 1, 2 \tag{10b}$$

where a and b are the semi-major and semi-minor axes, respectively, of the elliptical boundary. Corresponding to (10a-b) are the inverse mapping functions

$$z = (a+b)\,\zeta/2 + (a-b)\,/\,2\zeta \tag{11a}$$

$$z_k = (a-i\mu_k b)\,\zeta_k/2 + (a+i\mu_k b)\,/2\zeta_k \qquad k = 1, 2 \tag{11b}$$

which map the problem from the ζ- and ζ_k-planes onto the z- and z_k-planes, respectively. In the ζ_k-planes, the stress functions have the general form

$$\Phi_k(\zeta_k) = A_k \ell n \zeta_k + \sum_{-\infty}^{\infty} A_{km} \zeta_k^{-m} \qquad k = 1, 2 \tag{12}$$

consisting of a Laurent series expansion and a logarithmic term which admits the possibility of net loads on the elliptical boundary.

The A_k and A_{km} of (12) are determined from boundary conditions. The tractions on the elliptical boundary, which are chosen to cancel the uniform stress field of the first sub-problem, are clearly self-equilibrating, so

$$A_k = 0 \qquad k = 1, 2 \tag{13}$$

No remote loading is present, so it may be concluded that

$$\lim_{z_k \to \infty} \Phi_k'(z_k) = 0 \qquad k = 1, 2$$

or, since (10a-b) are affine

$$\lim_{\zeta_k \to \infty} \Phi_k'(\zeta_k) = 0 \qquad k = 1, 2 \tag{14}$$

It follows from (14) that

$$A_{km} = 0 \qquad k = 1, 2 \tag{15}$$

for $m \leq -1$. Furthermore, it may be seen from (5a-b) that the A_{k0} represent rigid body motions; these values may therefore be arbitrarily set equal to zero, without affecting the elasticity solution.

The as yet unspecified values of the A_{km} for $m \geq 1$ are determined from the tractions on the mapped elliptical boundary, using the relations

$$2Re[\Phi_1(\zeta_1) + \Phi_2(\zeta_2)] = -\int T_y ds + \lambda_1 \tag{16a}$$

$$2Re[\mu_1\Phi_1(\zeta_1) + \mu_2\Phi_2(\zeta_2)] = \int T_x ds + \lambda_2 \tag{16b}$$

where T_x and T_y are the components of the traction vector on the physical elliptical boundary, ds is a positively directed segment of the mapped elliptical boundary in the ζ-plane, and λ_1 and λ_2 are arbitrary constants of integration. The traction integrals are evaluated on the mapped elliptical boundary, and expressed as general Fourier series,

$$-\int T_y ds = \sum_1^\infty [a_m e^{im\Theta} + c_m e^{-im\Theta}] \tag{17a}$$

$$\int T_x ds = \sum_1^\infty [b_m e^{im\Theta} + d_m e^{-im\Theta}] \tag{17b}$$

Evaluating the stress functions on the mapped elliptical boundary (which, as noted above is the unit circle, $\zeta = \zeta_k = e^{i\Theta}$) yields

expressions for $\Phi_k(\zeta_k)$

$$\Phi_k(\zeta_k) = \sum_1^\infty A_{km} e^{-im\theta} \qquad k = 1, 2 \tag{18}$$

which are valid only on the mapped elliptical boundary.

Substituting (17a-b) and (18) into (16a-b) yields equations which are written solely in series of powers of $e^{i\theta}$. The A_{km} may then be evaluated by equating coefficients of like powers of $e^{i\theta}$.

$$A_{1m} + A_{2m} = c_m \tag{19a}$$

$$\bar{A}_{1m} + \bar{A}_{2m} = a_m \tag{19b}$$

$$\mu_1 A_{1m} + \mu_2 A_{2m} = b_m \tag{19c}$$

$$\bar{\mu}_1 \bar{A}_{1m} + \bar{\mu}_2 \bar{A}_{2m} = d_m \tag{19d}$$

$$\lambda_1 = \lambda_2 = 0 \tag{19e}$$

It is clear, from (19a-d), that

$$a_m = \bar{c}_m \tag{20a}$$

$$b_m = \bar{d}_m \tag{20b}$$

and, as a result, only two of (19a-d) are independent equations in A_{km}. Solving either pair of independent equations yields

$$A_{1m} = (\mu_2 \bar{c}_m - \bar{d}_m) \; / \; (\mu_2 - \mu_1) \tag{21a}$$

$$A_{2m} = (\bar{d}_m - \mu_1 \bar{c}_m) \; / \; (\mu_2 - \mu_1) \tag{21b}$$

The stress functions may thus be written

$$\Phi_1(\zeta_1) = \sum_1^\infty [(\mu_2 \bar{c}_m - \bar{d}_m) \; \zeta_1^{-m}] \; / \; (\mu_2 - \mu_1) \tag{22a}$$

$$\Phi_2(\zeta_2) = \sum_1^\infty [(\bar{d}_m - \mu_1 \bar{c}_m) \; \zeta_2^{-m}] \; / \; (\mu_2 - \mu_1) \tag{22b}$$

where the $\bar{c}_m$ and $\bar{d}_m$ are as yet unevaluated.

In order to determine $\bar{c}_m$ and $\bar{d}_m$, it is necessary to evaluate the traction integrals (17a-b) in the ζ-plane. As noted above, T_x and T_y are known in the z-plane, since, when the first and second sub-problems are superposed, the elliptical boundary must be stress free. These values of T_x and T_y may be mapped into the ζ-plane, and the traction integrals may then be evaluated. However, that procedure is not necessary in the present case, since the elliptical angle Θ, used for the parametric description of the elliptical boundary in the z-plane,

$$x = a \cos\Theta$$

$$y = b \sin\Theta$$

is identical to the angle Θ used to describe the unit circle in the ζ-plane. Thus, T_x, T_y, and ds may all be expressed in terms of Θ, and the traction integrals may then be evaluated in the z-plane. Such an evaluation yields the result

$$\bar{c}_1 = -(\sigma_o/2) \sin\phi[a \sin\phi - ib \cos\phi] + i\tau_o b/2 \qquad (23a)$$

$$\bar{d}_1 = -(\sigma_o/2) \cos\phi[a \sin\phi - ib \cos\phi] + \tau_o a/2 \qquad (23b)$$

$$\bar{c}_m = \bar{d}_m = 0 \qquad m \geq 2 \qquad (23c)$$

The stress functions are now completely evaluated, in the form $\Phi_k(\zeta_k)$. However, the stresses are known only in terms of $\Phi_k'(z_k)$, which is easily obtained by the chain-rule

$$\Phi_k'(z_k) = \Phi_k'(\zeta_k) \; d\zeta_k/dz_k \qquad k = 1, 2 \qquad (24)$$

Substituting (23c), (22a-b), and (10b) into (24) yields the result

$$\Phi_1'(z_1) = (\bar{d}_1 - \mu_2 \bar{c}_1)\, \zeta_1^{-1} \,/\, (\mu_2 - \mu_1)\, \sqrt{z_1^2 - a^2 - \mu_1^2 b^2} \qquad (25a)$$

$$\Phi_2'(z_2) = (\mu_1 \bar{c}_1 - \bar{d}_1)\, \zeta_2^{-1} \,/\, (\mu_2 - \mu_1)\, \sqrt{z_2^2 - a^2 - \mu_2^2 b^2} \qquad (25b)$$

The solution of the second sub-problem is now firmly in hand, requiring only a simple application of algebra to obtain stresses, strains, and displacements. This solution will not, however, be further pursued, as the focus of this work is not upon the results of the problem as stated, but rather upon the limit of those results as b approaches zero, i.e., as the ellipse approaches a one-dimensional crack of length 2a.

As might be expected, the results of the first sub-problem are unaffected by the limiting process. Rather surprising, however, is the observation that the $\Phi_k(\zeta_k)$, as given in (22a-b) are not directly altered in the limit as b approaches zero. Indirectly, however, some changes do occur, both through the Fourier coefficients $\bar{c}_m$ and $\bar{d}_m$, which assume the forms

$$\bar{c}_1 = -(\sigma_o\, a/2)\, \sin^2\phi \qquad (26a)$$

$$\bar{d}_1 = -(\sigma_o\, a/2)\, \sin\phi\cos\phi + \tau_o\, a/2 \qquad (26b)$$

$$\bar{c}_m = \bar{d}_m = 0 \qquad m \geq 2 \qquad (26c)$$

and through the mapping function (10b) which has the form

$$\zeta_k = [z_k + \sqrt{z_k^2 - a^2}\,] \,/\, a \qquad k = 1, 2 \qquad (27)$$

in the limit as b approaches zero. Thus, the stress functions may now be written

$$\Phi_1(\zeta_1) = a[\sigma_o \sin\phi(\cos\phi-\mu_2\sin\phi)-\tau_o]\ \zeta_1^{-1}/2(\mu_2-\mu_1) \tag{28a}$$

$$\Phi_2(\zeta_2) = a[\tau_o-\sigma_o\sin\phi(\cos\phi-\mu_1\sin\phi]\ \zeta_2^{-1}/2(\mu_2-\mu_1) \tag{28b}$$

Similarly, in the limit as b approaches zero, (25a-b) become

$$\Phi_1'(z_1) = a[\tau_o-\sigma_o\sin\phi(\cos\phi-\mu_2\sin\phi)]\ \zeta_1^{-1}/2(\mu_2-\mu_1)\sqrt{z_1^2-a^2} \tag{29a}$$

$$\Phi_2'(z_2) = a[\sigma_o\sin\phi(\cos\phi-\mu_1\sin\phi)-\tau_o]\ \zeta_2^{-1}/2(\mu_2-\mu_1)\sqrt{z_2^2-a^2} \tag{29b}$$

The region of primary interest is a zone near the crack tip, so a polar coordinate system with the origin at the crack tip is now introduced (Figure 4). The polar and complex coordinates are related by

$$z = a + re^{i\theta} \tag{30a}$$

$$z_k = a + r(\cos\theta + \mu_k \sin\theta) \qquad k = 1, 2 \tag{30b}$$

Substituting (30b) into (27) yields

$$\zeta_k = 1 + (r/a)\ (\cos\theta+\mu_k\sin\theta) + \sqrt{(r/a)(\cos\theta+\mu_k\sin\theta)[2 + (r/a)(\cos\theta+\mu_k\sin\theta)]} \tag{31}$$

In keeping with the interest in a region close to the crack tip, it is assumed that $r/a \ll 1$. Thus, within the crack-tip region, (31) may be simplified to the approximate form,

$$\zeta_k = 1 + \sqrt{(2r/a)(\cos\theta+\mu_k\sin\theta)} \qquad k = 1, 2 \tag{32}$$

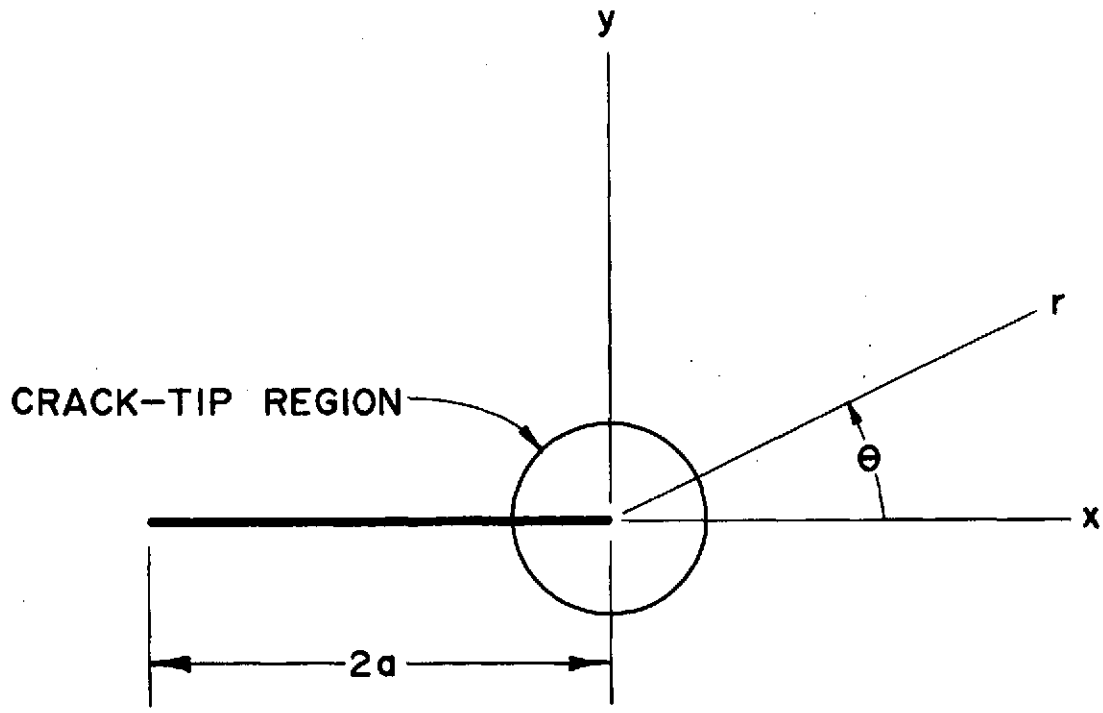

Figure 4. Coordinate systems for the crack-tip region. Stresses, strains, and displacements are expressed relative to the cartesian coordinates, as functions of the polar coordinates.

Inverting (32) and again simplifying the result by omitting higher order terms in r/a yields

$$\zeta_k^{-1} = 1 - \sqrt{(2r/a)(\cos\theta+\mu_k\sin\theta)} \qquad k = 1, 2 \tag{33}$$

The same simplification, i.e., dropping higher order terms in r/a, yields the approximate result

$$(z_k^2-a^2) = 1 / a\sqrt{(2r/a)(\cos\theta+\mu_k\sin\theta)} \qquad k = 1, 2 \tag{34}$$

Substituting (33) and (34) into (28a-b) and (29a-b) yields the approximate expressions

$$\Phi_1(z_1) = a[\sigma_o\sin\phi(\cos\phi-\mu_2\sin\phi) -\tau_o] [1 - \sqrt{(2r/a)(\cos\theta+\mu_1\sin\theta)}] / 2(\mu_2-\mu_1) \tag{35a}$$

$$\Phi_2(z_2) = a[\tau_o-\sigma_o\sin\phi(\cos\phi-\mu_1\sin\phi)][1 - \sqrt{(2r/a)(\cos\theta+\mu_2\sin\theta)}] / 2(\mu_2-\mu_1) \tag{35b}$$

and

$$\Phi_1'(z_1) = [\tau_o-\sigma_o\sin\phi(\cos\phi-\mu_2\sin\phi)][1-\sqrt{(2r/a)(\cos\theta+\mu_1\sin\theta)}] / 2(\mu_2-\mu_1)\sqrt{(2r/a)(\cos\theta+\mu_1\sin\theta)} \tag{36a}$$

$$\Phi_2'(z_2) = [\sigma_o\sin\phi(\cos\phi-\mu_1\sin\phi)-\tau_o][1-\sqrt{(2r/a)(\cos\theta+\mu_2\sin\theta)}] / 2(\mu_2-\mu_1)\sqrt{(2r/a)(\cos\theta+\mu_2\sin\theta)} \tag{36b}$$

It is again emphasized that (35a-b) and (36a-b) are valid only within the crack-tip region. Within this region, the stress and displacement fields for the general boundary conditions shown in Figure 1 may now be evaluated. However, a direct comparison of these

results to those obtained for an isotropic material is greatly facilitated if two special cases of the general remote loading shown in Figure 1 are considered.

II.5 Two special cases

The first special case of the general remote loading to be considered is mode I loading, which consists of remote uniform tension applied transverse to the crack. Mode I loading is clearly that instance of the general remote loading for which

$$\tau_o = 0 \tag{37}$$

$$\phi = \frac{\pi}{2} \tag{38}$$

Substituting (37) and (38) into (35a-b) and (36a-b) yields

$$\Phi_1(z_1) = -\sigma_o a\mu_2[1-\sqrt{(2r/a)(\cos\theta+\mu_1\sin\theta)}] \,/\, 2(\mu_2-\mu_1) \tag{39a}$$

$$\Phi_2(z_2) = \sigma_o\mu_1\,[1-\sqrt{(2r/a)(\cos\theta+\mu_2\sin\theta)}] \,/\, 2(\mu_2-\mu_1) \tag{39b}$$

and

$$\Phi_1'(z_1) = [\sigma_o\sqrt{a}\mu_2/2(\mu_2-\mu_1)][1-\sqrt{(2r/a)(\cos\theta+\mu_1\sin\theta)}]/\sqrt{2r(\cos\theta+\mu_1\sin\theta)} \tag{40a}$$

$$\Phi_2'(z_2) = -[\sigma_o\sqrt{a}\mu_1/2(\mu_2-\mu_1)][1-\sqrt{(2r/a)(\cos\theta+\mu_2\sin\theta)}]/\sqrt{2r(\cos\theta+\mu_2\sin\theta)} \tag{40b}$$

The complete, superposed stress and displacement fields in the crack-tip region are obtained by substituting (39a-b) and (40a-b) into (1a-c) and (5a-b), and adding the results to (8a-c) and (9a-b).

This procedure yields

$$\sigma_x = (K_I/\sqrt{2\pi r})\, Re\{[\mu_1\mu_2/(\mu_2-\mu_1)][\mu_1/\sqrt{\cos\theta+\mu_1\sin\theta} - \mu_2/\sqrt{\cos\theta+\mu_2\sin\theta}]\} + (K_I/\sqrt{\pi a})\, Re\{\mu_1\mu_2\} \tag{41a}$$

$$\sigma_y = (K_I/\sqrt{2\pi r})\, Re\{[1/(\mu_2-\mu_1)][\mu_2/\sqrt{\cos\theta+\mu_1\sin\theta} - \mu_1/\sqrt{\cos\theta+\mu_2\sin\theta}]\} \tag{41b}$$

$$\tau_{xy} = (K_I/\sqrt{2\pi r})\, Re\{[\mu_1\mu_2/(\mu_2-\mu_1)][1/\sqrt{\cos\theta+\mu_2\sin\theta} - 1/\sqrt{\cos\theta+\mu_1\sin\theta}]\} \tag{41c}$$

$$u = \sigma_o a Re\{\beta_{11}\mu_1\mu_2-\beta_{12}\} + K_I\sqrt{2r/\pi}\, Re\{[1/(\mu_2-\mu_1)][\mu_2 p_1\sqrt{\cos\theta+\mu_1\sin\theta}-\mu_1 p_2\sqrt{\cos\theta+\mu_2\sin\theta}]\} + \sigma_o r[\beta_{12}\cos\theta+(\beta_{26}\sin\theta)/2] \tag{42a}$$

$$v = \sigma_o a Re\{\beta_{26}-\beta_{22}(\mu_1+\mu_2)/\mu_1\mu_2\} + K_I\sqrt{2r/\pi}\, Re\{[1/(\mu_2-\mu_1)][\mu_2 q_1\sqrt{\cos\theta+\mu_1\sin\theta}-\mu_1 q_2\sqrt{\cos\theta+\mu_2\sin\theta}]\} + \sigma_o r[\beta_{22}\sin\theta+(\beta_{26}\cos\theta)/2] \tag{42b}$$

where K_I is the mode I stress intensity factor. As in metals- based LEFM, K_I, defined by

$$K_I = \sigma_o\sqrt{\pi a} \tag{43}$$

is, at least for the unbounded geometry under consideration, a function of only the loading and crack length.

It is noted that the uniform displacement terms in (42a-b) are rigid body motions, and may therefore be neglected. Furthermore,

since $\sqrt{r} >> r$ within the crack-tip region, (42a-b) may be written in the simpler forms

$$u = K_I\sqrt{2r/\pi}\ Re\{[1/(\mu_2-\mu_1)][\mu_2 p_1\sqrt{\cos\theta+\mu_1\sin\theta} - \mu_1 p_2\sqrt{\cos\theta+\mu_2\sin\theta}]\} \quad (44a)$$

$$v = K_I\sqrt{2r/\pi}\ Re\{[1/(\mu_2-\mu_1)][\mu_2 q_1\sqrt{\cos\theta+\mu_1\sin\theta} - \mu_1 q_2\sqrt{\cos\theta+\mu_2\sin\theta}]\} \quad (44b)$$

The second special case to be considered is that of mode II loading, which consists of remote uniform shear. Mode II loading is clearly equivalent to the general loading shown in Figure 1 if

$$\sigma_o = 0 \quad (45)$$

Substituting (45) into (35a-b) and (36a-b) yields

$$\Phi_1(z_1) = -[\tau_o a/2(\mu_2-\mu_1)][1-\sqrt{(2r/a)(\cos\theta+\mu_1\sin\theta)}] \quad (46a)$$

$$\Phi_2(z_2) = [\tau_o a/2(\mu_2-\mu_1)][1-\sqrt{(2r/a)(\cos\theta+\mu_2\sin\theta)}] \quad (46b)$$

and

$$\Phi_1'(z_1) = \tau_o\sqrt{a}[1-\sqrt{(2r/a)(\cos\theta+\mu_1\sin\theta)}\ /2(\mu_2-\mu_1)\sqrt{2r(\cos\theta+\mu_1\sin\theta)}] \quad (47a)$$

$$\Phi_2'(z_2) = -\tau_o\sqrt{a}[1-\sqrt{(2r/a)(\cos\theta+\mu_2\sin\theta)}\ /2(\mu_2-\mu_1)\sqrt{2r(\cos\theta+\mu_2\sin\theta)}] \quad (47b)$$

The complete, superposed stress and displacement fields in the crack-tip region are obtained by substituting (46a-b) and (47a-b) into (1a-c) and (5a-b), and adding the resulting expressions to (8a-c) and (9a-b). This procedure yields

$$\sigma_x = (K_{II}/\sqrt{2\pi r})\ Re\{[1/(\mu_2-\mu_1)][\mu_1^2/\sqrt{\cos\theta+\mu_1\sin\theta} - \mu_2^2/\sqrt{\cos\theta+\mu_2\sin\theta}]\} + (K_{II}/\sqrt{\pi a})\ Re\{\mu_1+\mu_2\} \quad (48a)$$

$$\sigma_y = (K_{II}/\sqrt{2\pi r})\ Re\{[1/(\mu_2-\mu_1)][1/\sqrt{\cos\theta+\mu_1\sin\theta} - 1/\sqrt{\cos\theta+\mu_2\sin\theta}]\} \quad (48b)$$

$$\tau_{xy} = (K_{II}/\sqrt{2\pi r})\ Re\{[1/(\mu_2-\mu_1)][\mu_2\sqrt{\cos\theta+\mu_2\sin\theta} - \mu_1/\sqrt{\cos\theta+\mu_1\sin\theta}]\} \quad (48c)$$

$$\begin{aligned} u = {} & \tau_o a\ Re\{\beta_{11}(\mu_1+\mu_2) - \beta_{16}\} + \\ & K_{II}\sqrt{2r/\pi}\ Re\{[1/(\mu_2-\mu_1)][p_1\sqrt{\cos\theta+\mu_1\sin\theta} - p_2\sqrt{\cos\theta+\mu_2\sin\theta}]\} + \\ & \tau_o r[\beta_{16}\cos\theta + (\beta_{66}\sin\theta)/2] \end{aligned} \quad (49a)$$

$$\begin{aligned} v = {} & \tau_o a\ Re\{\beta_{22}(\mu_1+\mu_2)/\mu_1\mu_2 - \beta_{12}\} + \\ & K_{II}\sqrt{2r/\pi}\ Re\{[1/(\mu_2-\mu_1)][q_1\sqrt{\cos\theta+\mu_1\sin\theta} - q_2\sqrt{\cos\theta+\mu_2\sin\theta}]\} + \\ & \tau_o r[\beta_{26}\sin\theta + (\beta_{66}\cos\theta)/2] \end{aligned} \quad (49b)$$

where K_{II} is the mode II stress intensity factor. As in the instance of mode I loading, the mode II stress intensity factor

$$K_{II} = \tau_o \sqrt{\pi a} \quad (50)$$

is the same function of loading and crack length in both isotropic and anisotropic materials.

Simplification of the displacement expressions (49a-b) is again possible, since the uniform displacement terms represent rigid body motions, and the terms of order r are comparatively small within the crack-tip region. The simplified displacement expressions are

$$u = K_{II}\sqrt{2r/\pi}\ Re\{[1/(\mu_2-\mu_1)][p_1\sqrt{\cos\theta+\mu_1\sin\theta} - p_2\sqrt{\cos\theta+\mu_2\sin\theta}]\} \quad (51a)$$

$$v = K_{II}\sqrt{2r/\pi}\ Re\{[1/(\mu_2-\mu_1)][q_1\sqrt{\cos\theta+\mu_1\sin\theta} - q_2\sqrt{\cos\theta+\mu_2\sin\theta}]\} \quad (51b)$$

Stress and displacement fields within the crack-tip region have been obtained for both mode I and mode II loading. Some comparisons of these anisotropic results to the results obtained from the analysis of identical problem geometries of an isotropic material are now both possible and appropriate.

II.6 Observations

Within the crack-tip region of an isotropic material, the stress and displacement fields may be shown to have the form [18]

$$\sigma_{ij} = (K_\xi/\sqrt{2\pi r})\ f_{ij}^{\xi}(\theta) + O[(r/a)^0] \quad i,j = 1, 2 \tag{52a}$$

$$u_i = K_\xi\sqrt{2r/\pi}\ g_i^{\xi}(\theta) + O[(r/a)^1] \quad i = 1, 2 \tag{52b}$$

where K_ξ is the stress intensity factor for mode ξ loading, $f_{ij}^{\xi}(\theta)$ is a mode dependent spatial distribution function, and $g_i^{\xi}(\theta)$ is a spatial distribution function which is both mode and material dependent. These same results in an anisotropic material, (41a-c), (44a-b), (48a-c), and (51a-b), may be written in the form

$$\sigma_{ij} = (K_\xi/\sqrt{2\pi r})\ h_{ij}^{\xi}(\theta;\mu_1,\mu_2) + O[(r/a)^0] \quad i,j = 1, 2 \tag{53a}$$

$$u_i = K_\xi\sqrt{2r/\pi}\ k_i^{\xi}(\theta;\mu_1,\mu_2) + O[(r/a)^1] \quad i = 1, 2 \tag{53b}$$

where $h_{ij}^{\xi}(\theta;\mu_1,\mu_2)$ and $k_i^{\xi}(\theta;\mu_1,\mu_2)$ are spatial distribution functions which are both mode and material dependent.

Comparison of (52a-b) and (53a-b) reveals some striking similarities and a major difference between the isotropic and anisotropic results. The stress and displacement fields exhibit the same functional

dependence on r in both types of material. Furthermore, the magnitudes of the stress and displacement fields are determined by the stress intensity factor in both isotropic and anisotropic materials. Indeed, the only significant difference between (52a-b) and (53a-b) is that the stress field within the crack-tip region is material dependent in anisotropic materials, but not in isotropic materials. As discussed in chapter III, this material dependence need cause no concern, as long as the stress intensity factors are not functions of material constants. Such is clearly the case for the unbounded geometry upon which the above analysis was based. However the form, and perhaps the very nature of the stress intensity factor are altered by the presence of finite external boundaries. It is therefore necessary to investigate the nature of the stress intensity factor for more realistic geometries than that considered above.

CHAPTER III

THE EFFECTS OF FINITE BOUNDARIES

III.1 Introduction

It is shown in chapter II that the stresses and displacements within the crack-tip region have markedly similar forms in isotropic and anisotropic materials. This similarity implies that, as in isotropic materials, any of a number of physical criteria for characterizing crack growth in anisotropic materials (e.g., stress, displacement, or energy levels) may be stated in terms of the stress intensity factor. It follows, then, that the satisfaction of any of these physical criteria, as indicated by actual crack growth, corresponds to some specific value of the appropriate stress intensity factor in a given material. It is emphasized that this specific value of the stress intensity factor, herein referred to as fracture strength, is a material parameter, and therefore quite different from the stress intensity factor *per se*, an analytical construct.

One consequence of the above distinction between fracture strength and the stress intensity factor is that, while the latter may be calculated, the former must be experimentally determined. These experimental measurements are obtained by loading a pre-cracked specimen, typically under mode I conditions, until crack growth occurs; the stress intensity factor, as calculated for the conditions corresponding to the observed initiation of crack growth, is the fracture strength of the

material being tested. This procedure obviously requires the calculation of the stress intensity factor for a finite specimen configuration, which in turn necessitates some modification of the stress intensity factor defined in chapter II for an unbounded geometry. This modification is accomplished by means of a finite correction factor Y, i.e.,

$$K_I = \sigma_0 Y\sqrt{a} \tag{54}$$

for a finite specimen configuration subjected to mode I loading. Values of Y have been numerically calculated for a number of standard isotropic test specimen configurations [19]; these calculations have demonstrated that Y is a function of only the specimen geometry in isotropic materials.

Because the finite correction factor is based on pragmatic, rather than theoretical considerations, its character in anisotropic materials is open to question. In particular, the possibility of a material dependent finite correction factor arises with the consideration of anisotropic media [20]. Material dependence would, of course, substantially reduce the utility of the finite correction factor concept, as Y would have to be calculated on a case-by-case basis. In view of the significance of the anisotropic finite correction factor, an investigation of its character is clearly appropriate. One such investigation is described below.

III.2 Analysis

The investigation of the anisotropic finite correction factor was performed by analyzing the center-cracked tension coupon configuration shown in Figure 5, for both a number of fiber composite laminates and a single isotropic material. The parameters considered in this study are the specimen dimensions and laminate construction (Table I) and the material properties of the basic composite plies (Table II). All of the composite laminates in the analytical program are specially orthotropic (i.e., they exhibit no tension-shear coupling) and mid-plane symmetric. The homogeneous material models of these laminates obtained from lamination theory thus correspond to the material model used in chapter II, with the additional restriction that β_{16} and β_{26} are zero.

The analysis was performed numerically, using either an isotropic or anisotropic implementation (as appropriate) of the boundary-integral equation solution technique [21]. This particular solution method was chosen because it requires discrete modelling of only the specimen boundary, and not the specimen interior. This feature naturally leads to a reduction in problem size and solution time. The inherent effiency of the solution method was furthered by the symmetry of both the specimen configuration and the materials of interest with respect to the crack. This symmetry permitted the modelling of the plane ahead of the crack as an external boundary. Thus, stress data along

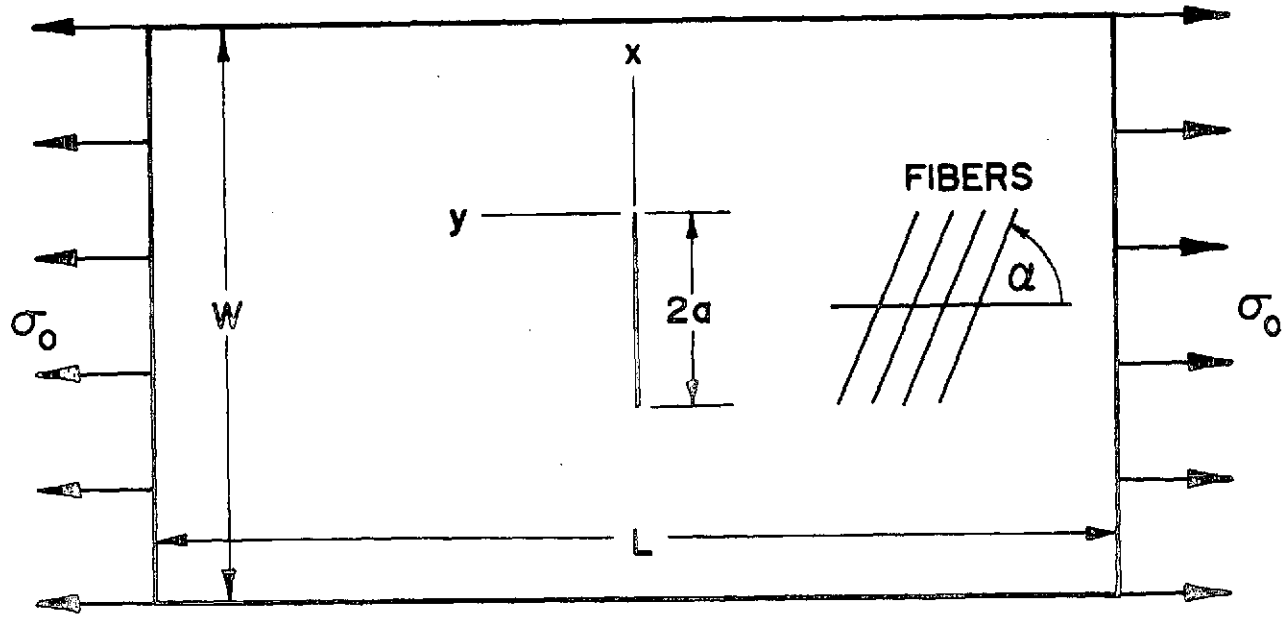

Figure 5. Center-cracked tension specimen. The fiber orientation angle, α, is variable as are the specimen dimensions, L, W, and a (see Table I).

Table I

Specimen Description

Specimen Type I:

L = 10.5 in.
W = 3.5 in.
a = 0.125 in.; 0.250 in.; 0.500 in.
$\alpha = (0°)_s; (90°)_s; (\pm 45°)_s$
Material system: Boron/epoxy

Specimen Type II:

L = 10.0 in.
W = 6.0 in.
a = 1.0 in.
$\alpha = (0°)_s; (\pm 15°)_s; (\pm 30°)_s; (\pm 45°)_s; (\pm 60°)_s;$
$(\pm 75°)_s; (90°)_s$
Material system: Graphite/epoxy

Specimen Type III:

L = 5.0 in.
W = 1.0 in.
a = 0.1250 in.; 0.1875 in.; 0.2500 in.
$\alpha = (0_4^\circ/\pm 45°)_s; (0°/\pm 45°)_s; (0°/\pm 45°/90°)_s$
Material system: Boron/epoxy; isotropic material

Specimen Type IV:

L = 9.9 in.
W = 2.5 in.
a = 0.5 in.
$\alpha = (0_4^\circ/\pm 45°)_s; (0°/\pm 45°)_s; (0°/\pm 45°/90°)$
Material system: Boron/epoxy; isotropic material

Table II

Material Properties

Boron/epoxy:

$$E_{11} = 30.0 \times 10^6 \text{ lb/in}^2$$
$$E_{22} = 2.70 \times 10^6 \text{ lb/in}^2$$
$$G_{12} = 0.65 \times 10^6 \text{ lb/in}^2$$
$$\nu_{12} = 0.21$$

Graphite/epoxy:

$$E_{11} = 21.0 \times 10^6 \text{ lb/in}^2$$
$$E_{22} = 1.70 \times 10^6 \text{ lb/in}^2$$
$$G_{12} = 0.65 \times 10^6 \text{ lb/in}^2$$
$$\nu_{12} = 0.21$$

Isotropic material:

$$E = 30.0 \times 10^6 \text{ lb/in}^2$$
$$G = 11.5 \times 10^6 \text{ lb/in}^2$$
$$\nu = 0.30$$

Note: Material properties of the composite laminates were calculated from the lamina properties listed above, using the procedures described in [16].

this line was generated as part of the boundary solution, without the use of the slower interior solution portions of the program.

The specimen models used for this work, though similar in form, varied somewhat in detail according to specimen type and crack length. The models were composed of from fifty to seventy boundary segments, each segment having two degrees of freedom. Load was introduced into the specimen models by displacement boundary conditions. Solution times varied with problem size, from roughly 25 to 55 seconds on a Univac 1108 computer.

The data obtained from the numerical analysis were reduced according to a procedure described in [22]. This procedure is based on the observation that for mode I loading, the transverse stress on the crack axis has the same form in isotropic and anisotropic materials, namely

$$\sigma_y(r,0°) = K_I/\sqrt{2\pi r} + O[(r/a)°] \tag{55}$$

Substituting (54) into (55) yields, after some manipulation, the expression

$$\sigma_y\sqrt{r}/\sigma_0\sqrt{a} = Y/\sqrt{2\pi} + O[(r/a)^{1/2}] \tag{56}$$

which becomes, in the limit as r/a approaches zero,

$$Y = \sqrt{2\pi} \lim_{r/a\to 0} \sigma_y\sqrt{r} \,/\, \sigma_0\sqrt{a} \tag{57}$$

Values of the finite correction factor may be extracted from the numerical data by evaluating (57) with a graphical technique.

The graphical procedure consists of plotting the numerical data in the form $\sigma_y\sqrt{r}$ / $\sigma_0\sqrt{a}$ vs. r/a (Figure 6). As might be expected, the data points exhibit a substantial amount of scatter for small values of r/a, as the basic numerical results deteriorate somewhat close to the stress singularity at the crack tip. However, over a rather large range of values of r/a, the data behave linearly. A straight line is fitted to the data in this region, and extrapolated back to r/a = 0. As indicated by (57) and Figure 6, the intercept of this extrapolated curve is equal to $Y/\sqrt{2\pi}$.

III.3 Results and observations

Values of Y were obtained for each of the specimens listed in Table I, with the exception of the three $(\pm 45°)_s$ Type I specimens. (For reasons discussed below, the data for these specimens did not follow a set pattern when plotted against r/a.) A value of Y*, the finite correction factor for isotropic center-cracked tension coupons, was also calculated for each specimen configuration. As stated above, Y* is a function of specimen geometry only, having the form [19]

$$Y^* = 1.77 + 0.227(2a/W) - 0.510(2a/W)^2 + 2.7(2a/W)^3 \qquad (58)$$

where a and W are specimen dimensions (Figure 5). It is emphasized that values of Y* obtained from (58) are distinct from those values of Y calculated by numerical analysis of isotropic specimens.

Values of Y and Y* are listed in Table III, and shown graphically

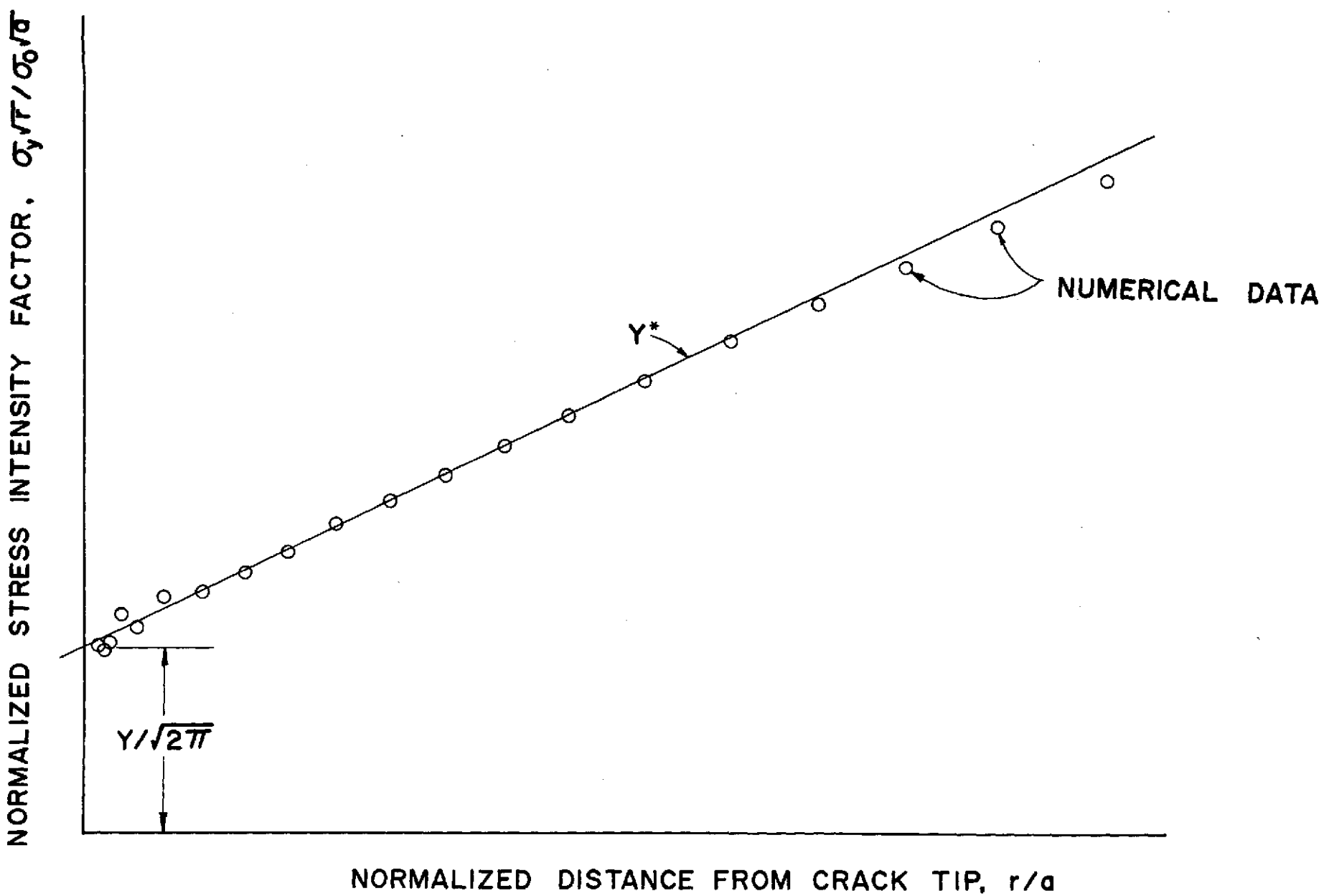

Figure 6. Graphical procedure for calculating the finite correction factor.

Table III

Finite Correction Factors

Specimen Type I

a	$\alpha = (0°)_s$		$\alpha = (90°)_s$		$\alpha = (\pm 45°)_s$		Y*
	Y	Y/Y*	Y	Y/Y*	Y	Y/Y*	
0.125	1.780	0.997	1.787	1.001	—	—	1.785
0.250	1.772	0.984	1.792	0.996	—	—	1.800
0.500	1.792	0.965	1.855	0.999	—	—	1.856

Specimen Type II

a	$\alpha=(0°)_s$		$\alpha=(\pm 15°)_s$		$\alpha=(\pm 30°)_s$		$\alpha=(\pm 45°)_s$		$\alpha=(\pm 60°)_s$		$\alpha=(\pm 75°)_s$		$\alpha=(90°)_s$		Y*
	Y	Y/Y*	Y	Y/Y*	Y	Y/Y*	Y	Y/Y*	Y	Y/Y*	Y	Y/Y*	Y	Y/Y*	
1.000	1.845	0.977	1.865	0.987	1.983	1.050	1.968	1.042	1.938	1.026	1.884	0.997	1.867	0.988	1.889

TABLE III

FINITE CORRECTION FACTORS

(Continued)

Specimen Type III

a	$\alpha=(0_4^\circ/\pm 45^\circ)_s$		$\alpha=(0^\circ/\pm 45^\circ)_s$		$\alpha=(0^\circ/\pm 45^\circ/90^\circ)_s$		Isotropic		Y*
	Y	Y/Y*	Y	Y/Y*	Y	Y/Y*	Y	Y/Y*	
0.1250	1.805	0.983	1.712	0.932	1.760	0.958	1.827	0.995	1.837
0.1875	1.880	0.976	1.780	0.924	1.822	0.946	1.923	0.998	1.926
0.2500	2.010	0.960	1.980	0.946	1.960	0.936	2.073	0.990	2.094

Specimen Type IV

a	$\alpha=(0_4^\circ/\pm 45^\circ)_s$		$\alpha=(0^\circ/\pm 45^\circ)_s$		$\alpha=(0^\circ/\pm 45^\circ/90^\circ)_s$		Isotropic		Y*
	Y	Y/Y*	Y	Y/Y*	Y	Y/Y*	Y	Y/Y*	
0.500	1.943	0.995	1.968	1.008	1.943	0.995	1.938	0.993	1.952

Note: The values termed isotropic (Specimen Type III and Type IV) were calculated from numerical data, and must be distinguished from Y*.

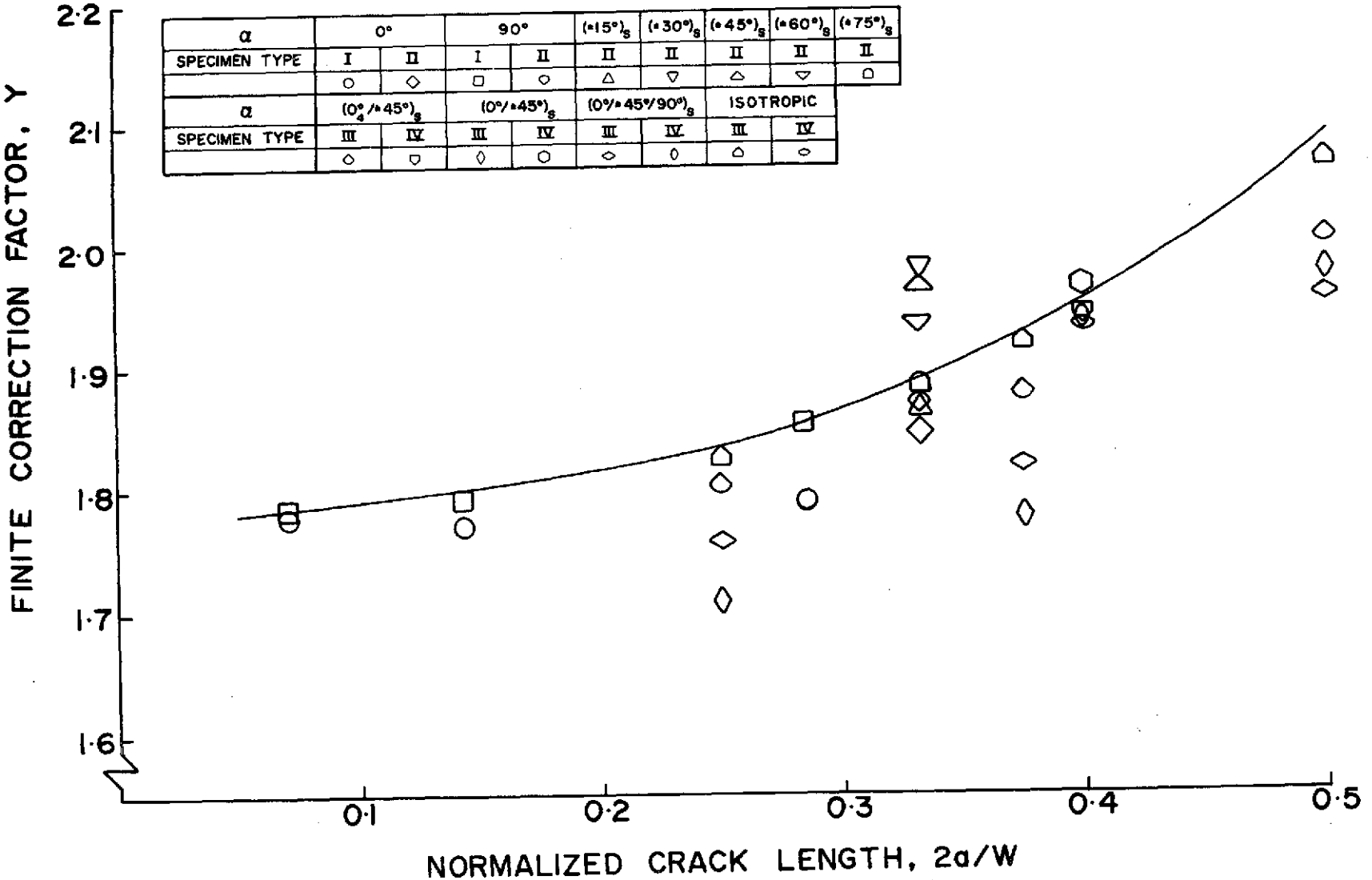

Figure 7. Finite correction factor vs. normalized crack length for the center-cracked tension specimen.

in Figure 7. Some slight variation of the finite correction factor is evident among specimens of different materials, but common specimen geometry. In most cases, the observed variation in Y is so small as to be neglible in the experimental context in which the finite correction factor is used. Of course, Y may exhibit larger variations for specimen configurations and/or materials other than those considered here, but there is no *a priori* reason for expecting such changes to occur, so long as no curved boundaries are present.[1]

Although the observed variation in the anisotropic finite correction factor is generally very small (less than eight per cent), it also seems to be very real, in spite of the approximate nature of the analysis techniques employed in this study. Indeed, a comparison of the values of Y calculated for the isotropic Type III and Type IV specimens with the appropriate values of Y* (Table III) indicates that the analysis method is actually quite accurate. The level of accuracy achieved in these examples is, moreover, considered to be representative of the accuracy of the solution technique in general, as the same analysis method was consistently applied throughout this work. Thus, it seems that the anisotropic finite correction factor is indeed material dependent, though the effects of the material dependence, as noted

[1]Because of the stress concentration associated with a curved boundary, such a boundary does influence the value of the stress intensity factor [23]. Since stress concentrations are material dependent in anisotropic media [17],it follows that the stress intensity factor will exhibit similar behavior in such media, if curved boundaries are present.

above, appear to be small for the particular specimen configuration and materials considered in this chapter. This conclusion is supported by the results of a more comprehensive study of the anisotropic finite correction factor, in which a specialized formulation of the boundary-integral equation method was employed [24]. The results of this larger study also indicate that, as noted above, the variation between the isotropic and anisotropic finite correction factors is real but generally small.

The specimen geometry of greatest interest to this work is the single edge-cracked specimen loaded in bending (see chapter IV). This specimen cannot presently be accurately analyzed by either the specialized or general boundary-integral equation methods, which model bending problems very poorly. However, the results of some finite element analyses (see chapter V) indicate that, for a $(\pm 45°)_s$ graphite/epoxy bend specimen, the isotropic and anisotropic finite correction factors differ by approximately ten per cent. It is noted that the variation between the two finite correction factors is a maximum for this particular laminate [24], and that the amount of variation is artificially high, due to the crude finite element model employed. Thus, although the anisotropic finite correction factor does appear to be somewhat material dependent, the isotropic finite correction factor does seem to be a reasonably accurate estimate under most conditions.

The observed interaction between the material properties of a

$(\pm 45°)_s$ laminate and specimen geometry may also serve to explain the behavior of the $(\pm 45°)_s$ Type I specimens. In this case, the critical aspect of the specimen configuration appears to be crack size, which is rather small in relation to the width of the Type I specimen. It is posited that the Type I specimen configuration does not, in fact, contain a crack of sufficient size to dominate the properties of a $(\pm 45°)_s$ laminate. This hypothesis is supported not only by experience in the analysis of cracks in metallic alloys, but also by the fact that the data for the $(\pm 45°)_s$ Type I specimens did improve somewhat with increasing crack size.

III.4 Conclusions

The nature of the anisotropic finite correction factor is clearly a topic requiring a great deal of further investigation. It is, however, obvious that this parameter can exhibit some material dependence for certain combinations of specimen geometry and laminate properties, though the isotropic finite correction factor is at least a good engineering estimate.

As a result, the isotropic finite correction factor is assumed to be applicable to the combinations of specimen geometry and laminate properties considered in the following chapters.

CHAPTER IV

AN EXPERIMENTAL STUDY

IV.1 Introduction

The results of the analytical and numerical studies described in chapters II and III indicate that many of the characteristic traits of isotropic fracture problems are unaffected by the introduction of material anisotropy. In particular, the stress and displacement fields within the crack-tip region exhibit the same dependence on K, the stress intensity factor, and r, the radial distance from the crack tip, in both isotropic and anisotropic materials. Moreover, K is essentially the same function of loading and geometry for finite configurations of isotropic and specially orthotropic anisotropic materials.

While such studies are clearly indicative of the potential applicability of metals-based LEFM to fiber composite laminates, they are hardly conclusive. As is the case with any attempt to characterize material behavior, analytical studies must be supplemented by observations of actual material response. Such observations are especially necessary in this instance, as the heterogeneity of fiber composites is completely disregarded in the material model used for the analytical and numerical work. In order to obtain the requisite data on actual material behavior, a pilot test program was performed.

This experimental program was designed to answer three closely related questions:

(i) Does a pre-existing crack in a fiber composite laminate propagate as a single entity, or does it become diffused into a number of cracks between and within the individual plies?

(ii) If the crack does grow without diffusing, is the direction of crack growth determined by the pre-existing crack or by the anisotropy and heterogeneity of the material?

(iii) Can metals-based LEFM be applied to fiber composite materials, i.e., is the fracture strength of a fiber composite laminate a material parameter?

IV.2 Test procedures and program

In view of the objectives of the test program, it was clear that the experimental procedures should follow those developed within the framework of metals-based LEFM. Such procedures exist in the form of a rigorously prescribed test method [25], and extensive interpretations [19,26] of both the test method and the results. The test method specified in [25] was followed as closely as possible in this experimental program, though the nature of fiber composites (or simple practicality) did dictate some minimal deviations from the standard scheme.

The three-point bend specimen (Figure 8) was chosen for the test program, largely to avoid problems associated with gripping the test piece. The extensive use of this specimen configuration for fracture testing of metals has shown that the loading arrangement (particularly, the bearing load opposite the crack front) does not unduly influence the process of crack growth. In fact, the data reduction scheme prescribed for this specimen [25] accounts for the details of specimen geometry and loading arrangement.

The specimen configuration shown in Figure 8 follows the recommendations of [25] in all respects except the final sharpening of the crack. Such sharpening is accomplished in metal specimens by low amplitude cyclic loading of the specimen, which eventually produces a small sharp crack at the tip of a machined notch. As such loading may cause specimen delamination, rather than crack growth, in composite laminates, fatigue sharpening of the composite specimens was not attempted. Instead, the initial notch in the composite specimens was produced by sharpening a sawcut using an ultrasonic cutter. As may be seen in Figure 8, the resulting notch is sharp enough, at least near the tip, to closely approximate the one-dimensional flaw considered in the analytical work.

The specimens were arranged for testing as shown in Figure 9, where the specimen is centered on two parallel rollers of one-inch diameter, located with centerlines four inches apart. A third roller,

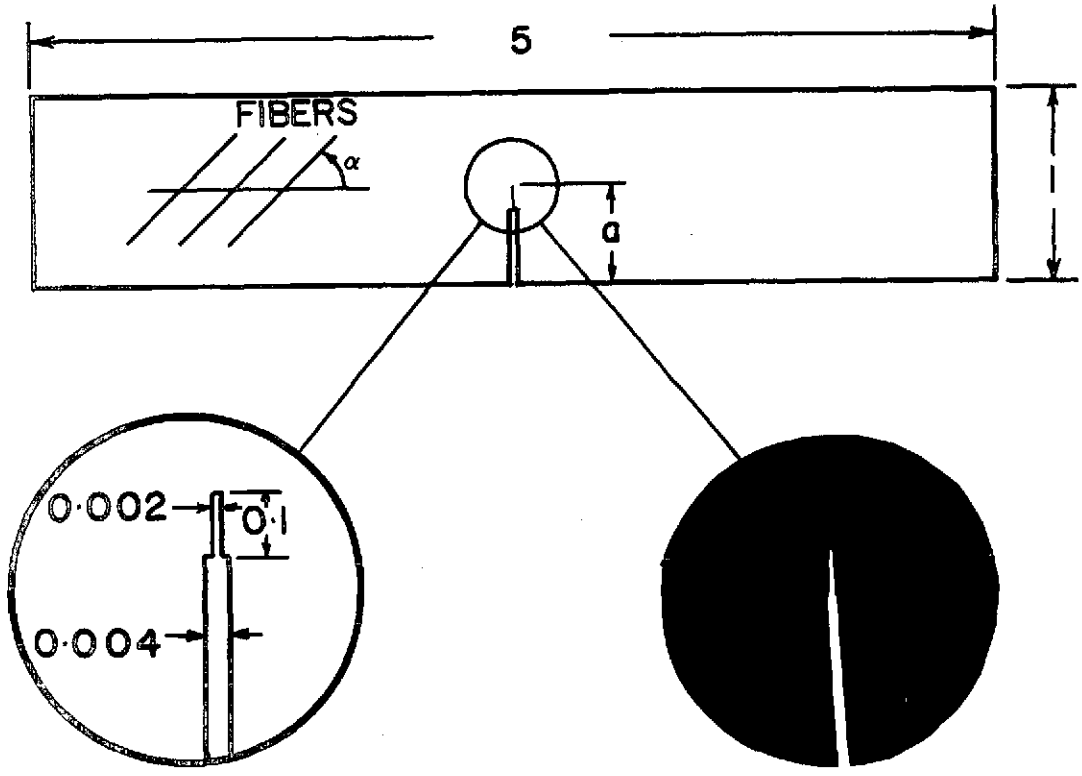

Figure 8. Three-point bend specimen geometry, with crack shape shown in inserts, both schematic (left) and actual (right). Fiber orientation angle, α, and crack length, a, are variable (see text). Nominal specimen thickness is 0.5 inch. All dimensions in inches.

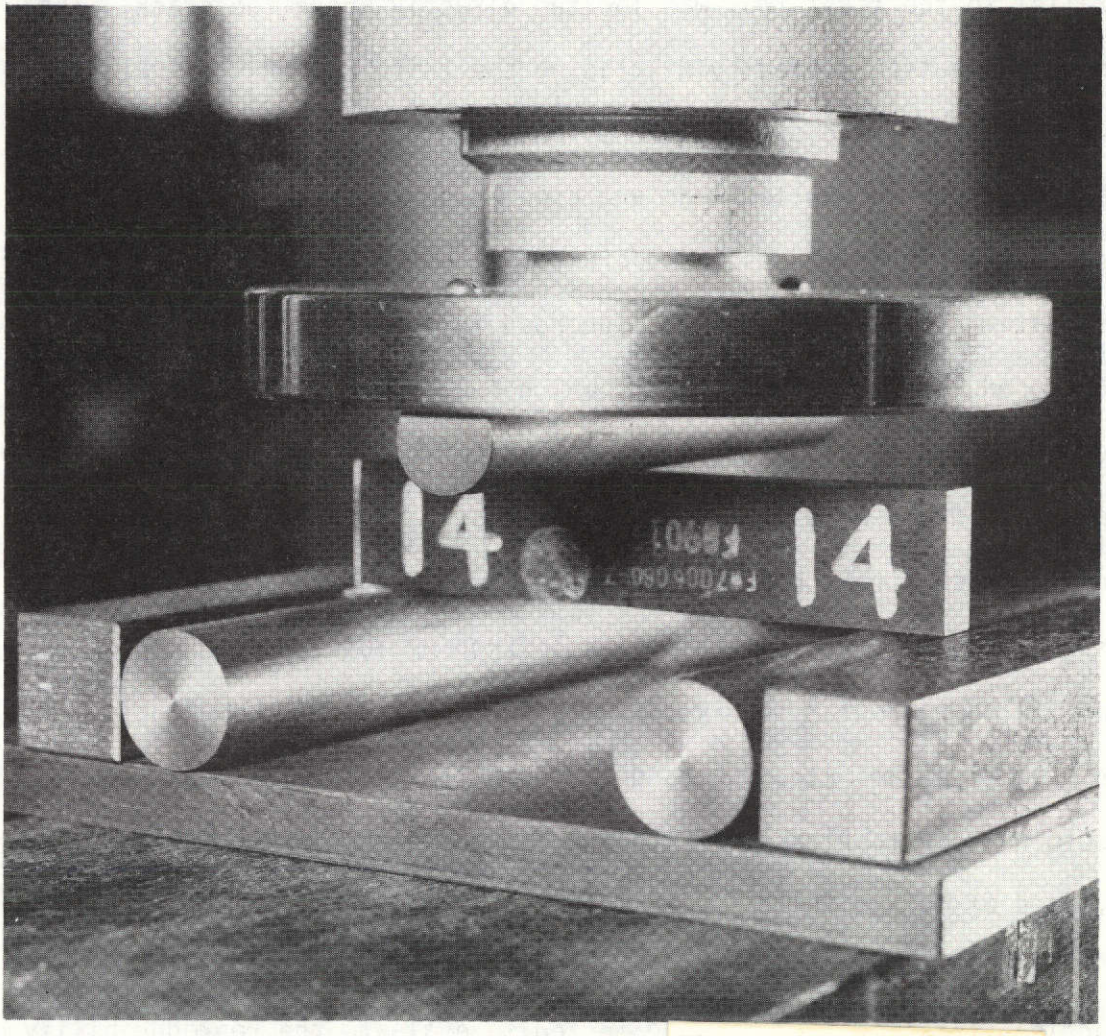

This page is reproduced at the back of the report by a different reproduction method to provide better detail.

Figure 9. Specimen in test jig at the beginning of loading.

parallel to the first two, was located directly above the crack. The specimen was then loaded by displacing the third roller vertically downward at the rate of 0.01 inches per minute, to minimize dynamic loading effects. Applied load and cross-head displacement were monitored during each test, and cross plotted to provide the basic test data. These data were not recorded in strict agreement with the procedures specified in [25], which require that crack mouth opening be monitored, rather than the motion of the loading head. The use of cross-head displacement was justified by the basically linear stress-strain behavior of composite laminates, and the use of a relatively stiff test machine (an Instron of 10,000 pound capacity).

The test program involved twenty-three specimens, covering a range of five laminate types and three initial notch lengths. All specimens were fabricated of a NARMCO graphite/epoxy material system, composed of Morganite II fibers in 5206 resin.

Included in the experimental program were two sets of five identical specimens, which were tested to evaluate the reproducibility of the results. One such set was a unidirectional laminate (α=0°) with an initial crack length of 0.4 inches. The other set was a multi-directional laminate ($\alpha = (0°/\pm 45°/90°)_s$) with the same initial crack length. Single specimens were tested for the unidirectional laminates α=0°, 45°, and 90°, and for the multi-directional laminates $\alpha=(\pm 45°)_s$ and $(0°/\pm 45°/90°)_s$. For each of these test laminates,

initial crack lengths of 0.2, 0.4, and 0.6 inches were included in the test program. It should be noted that the shortest of these initial crack lengths is less than the minimum prescribed for fracture testing of metals [25]. Such specimens were nevertheless included in the test program to allow any possible material dominance to develop as the crack became a less significant feature of the specimen configuration.

IV.3 Data reduction and results

A typical example of the basic test data, a plot of load vs. cross-head displacement, is shown in Figure 10. The initial region of this plot, a region of increasing positive slope, corresponds to the taking up of slack in the load train, and the development of bearing surfaces at the loading rollers. There follows a linear region, over which the specimen deforms elastically. A third region of decreasing positive slope follows the linear portion of the plot; the nonlinearity of this third region is attributed to the initiation and accumulation of irreversible damage in the specimen (e.g., plastic flow in metals). Finally, the load peaks and falls off as the test piece fails.

In order to calculate the fracture strength from the test data, it is necessary to determine the point on the data curve which corresponds to the initiation of crack growth in the specimen. A rather obvious choice for this point of initial crack growth is the peak of the test data curve, corresponding to a load P_{max}. The use

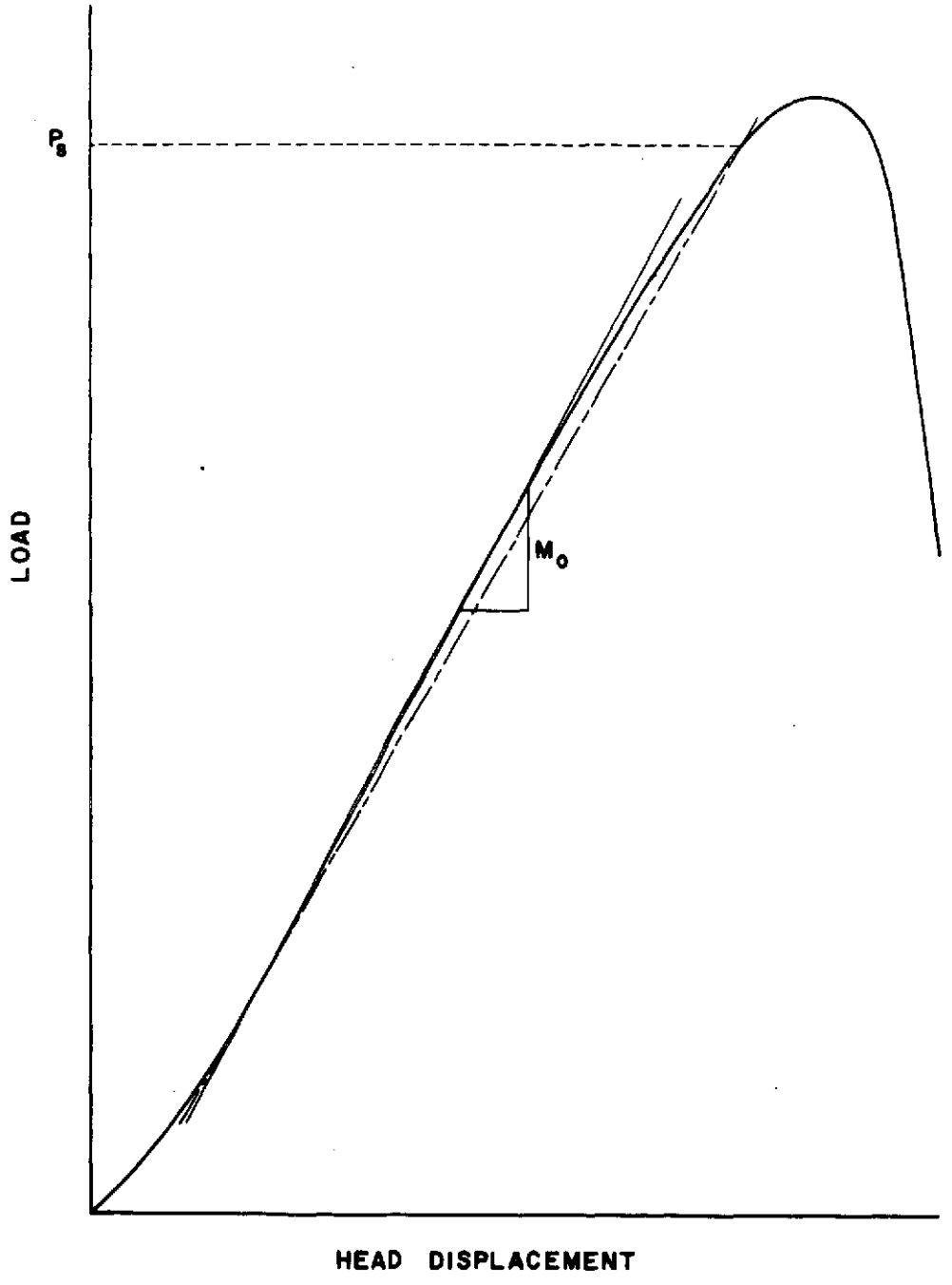

Figure 10. Typical plot of load applied to specimen vs. cross-head displacement, showing method used to determine P_S.

of this point is not, however, necessarily consistent with the linear elastic characterization of the crack-tip region, as a significant amount of nonlinear behavior such as slow crack growth may occur before the load-displacement curve reaches its peak. Only a limited amount of such behavior may be permitted if the linear elastic characterization of the crack-tip region is to be even an approximate description of the actual state of the specimen. Thus, the event of initial crack growth may be assigned to a point prior to the peak of the test data curve, in order to restrict the amount of nonlinear specimen behavior.

The appropriate point of initial crack growth may be determined by means of the following prescribed data reduction scheme [25]. The slope M_o of the linear portion of the load-displacement curve is identified, and a line of slope five per cent less than M_o is drawn from the initial point of the linear region of the data curve, as shown in Figure 10. This second line intercepts the load-displacement curve at some value of the load termed P_S. The load P_Q, which corresponds to the initiation of crack growth, is set equal to P_S if P_S is the greatest load withstood by the specimen to that point in the test. If, on the other hand, P_{max} precedes P_S on the data curve, P_Q is set equal to P_{max}[1]. In either case, experience in metals testing has

[1]The data reduction scheme specified in [25] is significantly more complex than the portion of that scheme described here. As the additional parts of the complete data reduction scheme are concerned with the occurrence of excessive plastic flow within the specimen, they are not applicable to the brittle composite laminates considered in this work.

shown P_Q to correspond to the point of initial crack growth.

The values of P_Q obtained via the above procedure were used in conjunction with the known specimen geometry to calculate K_Q, the candidate fracture toughness of a specimen. The value of K_Q was obtained from the relation [25]

$$K_Q = 3P_Q SY\sqrt{a}/2BW^2 \tag{59}$$

where S, B, and W are specimen dimensions (Figure 11) and Y is the isotropic finite correction factor [25]. It is noted that the formal validity of the test results could not be established, as strict compliance with the specifications of [25] requires, among other things, a yield strength for the test material. Thus, only candidate values of the fracture strength, and not the valid fracture toughness results denoted K_{Ic}, may be calculated from the test data.

The procedure described above was used to calculate a value of K_Q for each of the specimens successfully tested. These values are shown in Table IV, together with values of $\overline{K}_Q$, the average candidate fracture strength of a given laminate. Also of interest as test results are the failure surfaces of the various specimens, shown in Figures 12-16.

IV.4 Observations

The primary goal of a fracture test program is the determination of the fracture strength of a given material. While the calculation

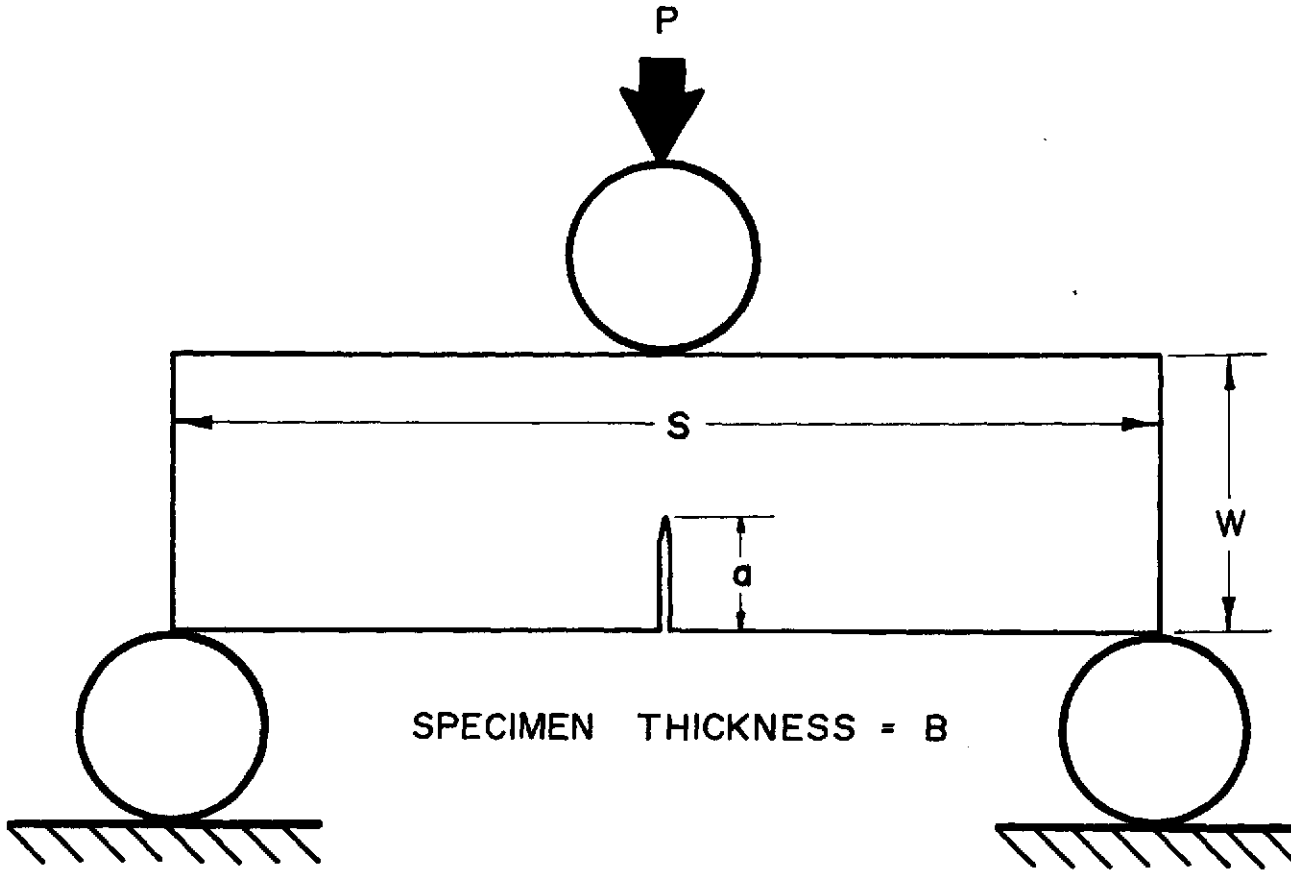

Figure 11. General notation for the three-point bend specimen configuration.

Table IV

Experimental Results

fiber orientation angle, α	K_Q, $lb/in^2\sqrt{in} \times 10^{-3}$ a=0.2 in	a=0.4 in	a=0.6 in	$\overline{K}_Q$, $lb/in^2\sqrt{in} \times 10^{-3}$	
0°	——[1]	28.8	36.3	32.6	+11% -11%
90°	1.66	1.46	——[2]	1.56	+6.3% -6.3%
45°	0.690[3]	2.22	2.39	2.30	+3.9% -3.8%
$(\pm 45°)_s$	18.5	18.5	16.3	17.7	+4.8% -9.4%
$(0°/\pm 45°/90°)_s$	23.5	21.7	20.5	21.9	+7.3% -8.6%

[1] Specimen was crushed before crack propagation occurred.

[2] Instrumentation failure.

[3] This value omitted when calculating $\overline{K}_Q$.

of K_Q is also a major objective of the experimental work described above, the exploratory nature of the test program suggests that more fundamental topics must also be addressed. In particular, the first two of the three questions posed at the outset of this program, concerning the nature and path of crack growth, must be considered.

The nature of crack growth in the specimens may be determined by inspection of the failure surfaces (Figures 12-16). Indeed, the fact that failure occurs on a single surface, however irregular, contrasts strongly with the fan-shaped region of damage typically encountered in fracture testing of fiberglass laminates [27]. The existence of a single fracture surface does not, however, necessarily indicate that crack growth occurred simultaneously along the entire crack front; in fact, the irregular topography of some of the failure surfaces suggests that the crack may have grown independently within the individual specimen plies. Evidence of such behavior has also been noted in a fractographic study of the failure surfaces [28]. However, except in the case of the unidirectional specimens for which $\alpha=0°$, independent crack growth was confined to a small region close to the crack tip, where the phenomenon may be interpreted as material damage accumulated prior to the initiation of unstable crack growth (see chapter VI). The actual initiation of crack instability occurred by simultaneous failure of all the specimen plies at a point on the boundary of the damaged region which is also quite close to the plane

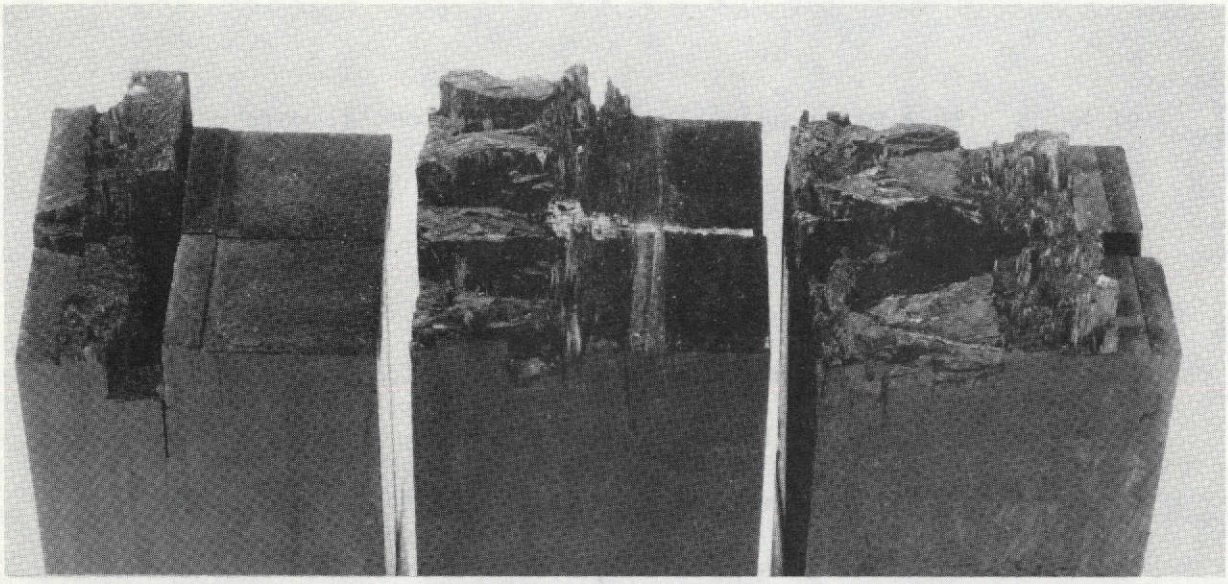

Figure 12. Failure surfaces for unidirectional 0° specimens of three starter crack lengths (a = 0.6, 0.4, 0.2 inch).

This page is reproduced at the back of the report by a different reproduction method to provide better detail.

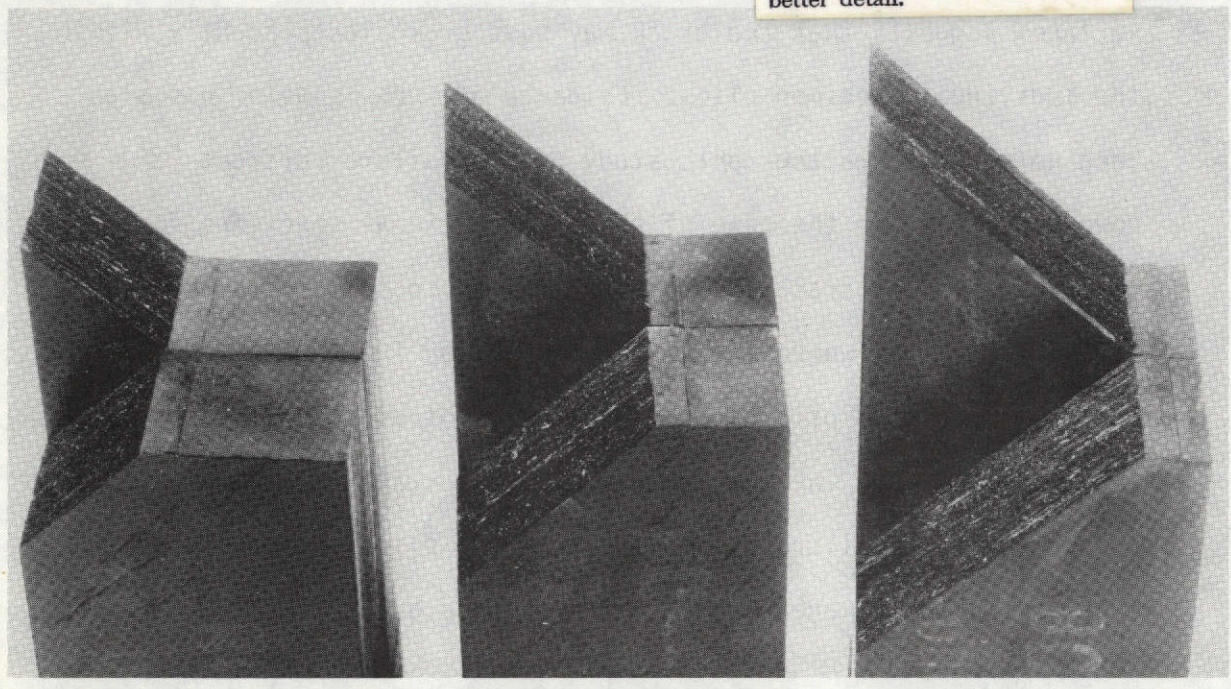

Figure 13. Failure surfaces for unidirectional 45° specimens of three starter crack lengths (a = 0.6, 0.4, 0.2 inch).

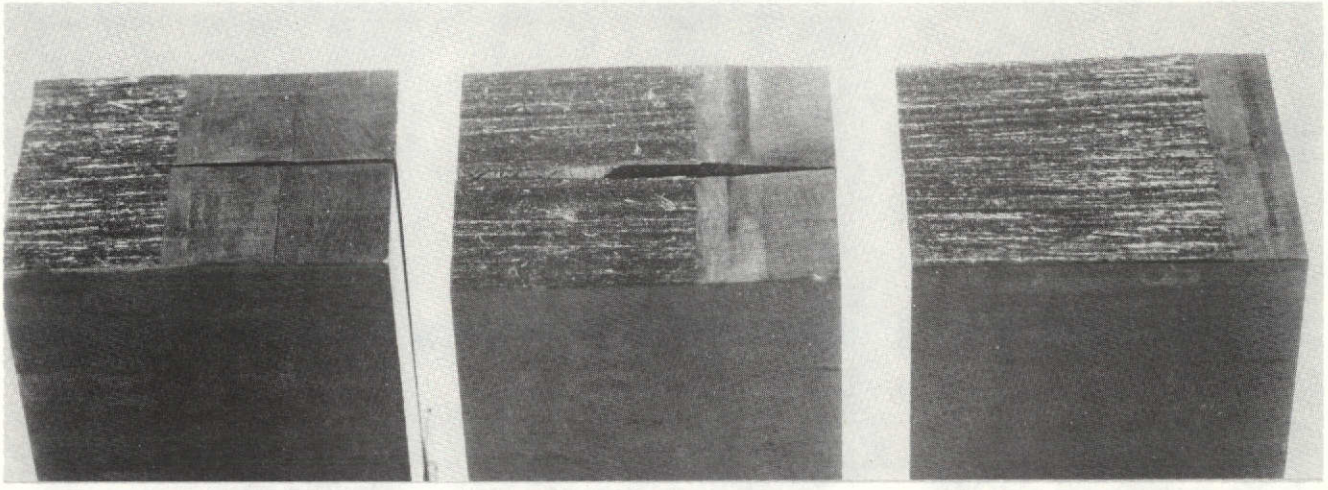

Figure 14. Failure surfaces for unidirectional 90° specimens of three starter crack lengths (a = 0.6, 0.4, 0.2 inch).

This page is reproduced at the back of the report by a different reproduction method to provide better detail.

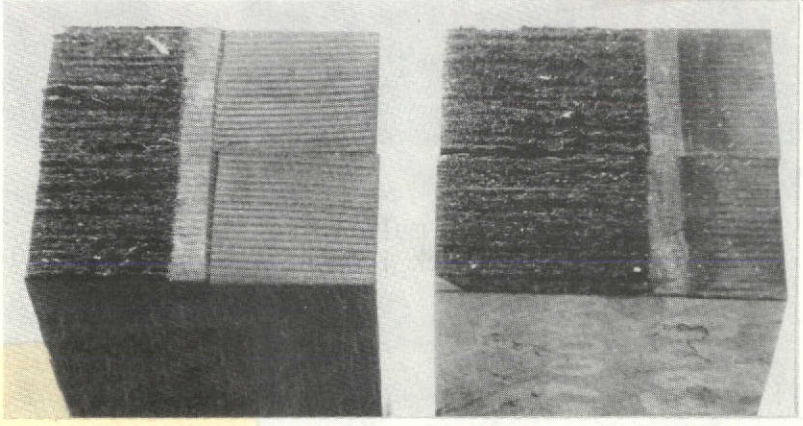

Figure 15. Failure surfaces for multi-directional $(0°/\pm45°/90°)_S$ specimens of two starter crack lengths (a = 0.6, 0.4 inch).

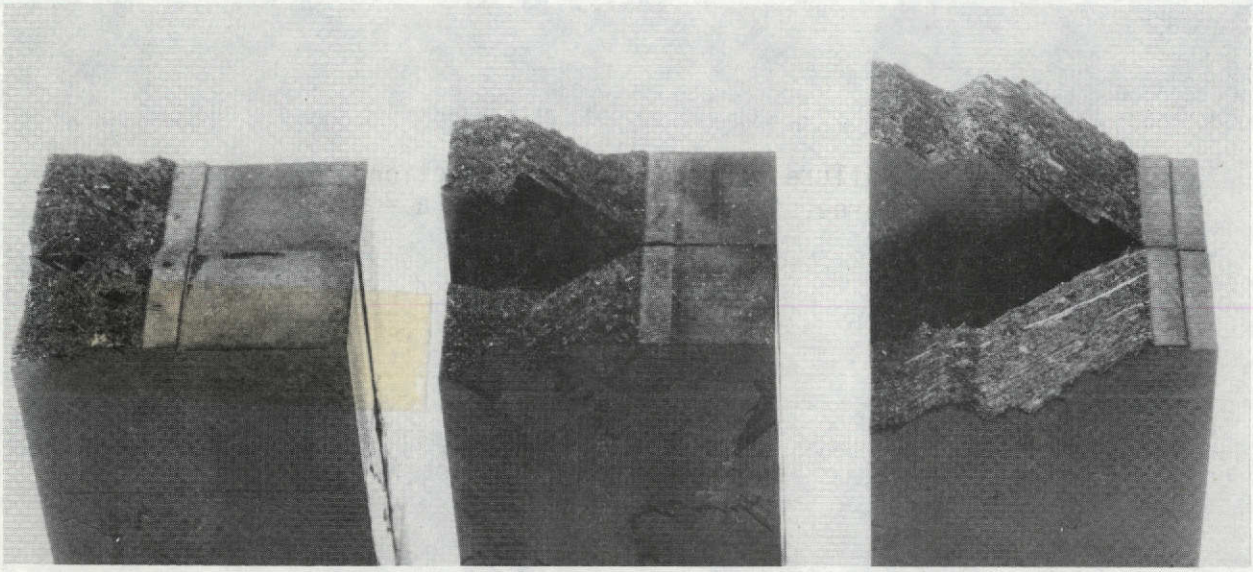

Figure 16. Failure surfaces for multi-directional $(\pm 45°)_s$ specimens of three starter crack lengths (a = 0.6, 0.4, 0.2 inch).

of the original crack. Thus, since the region of material damage due to independent crack growth is small at incipient crack instability — by reason of the data reduction scheme if not the physical behavior of the specimen — unstable crack growth in these specimens may be modelled as a single crack growing from the tip of the initial notch.

As implied above, a large amount of material damage accumulated prior to unstable crack growth in the unidirectional specimens for which $\alpha=0°$. This damage occurred in the form of secondary matrix cracks, which developed at and ahead of the tip of the starter crack, and grew between fibers. The extent to which such cracking occurred is evidenced by the failure surfaces shown in Figure 12, which indicate that, at failure, a substantial portion of the specimen ligament consists of virtually independent fiber bundles, separated by secondary matrix cracks. The development of these secondary cracks was quite noticeable during testing, as they were occasionally visible on the specimen surface and always accompanied by conspicuous "popping" sounds, thought to be indicative of matrix fracture.

The extensive amount of material damage indicated on the failure surfaces shown in Figure 12 suggests that a fracture strength calculation based on the maximum load on the test data curve will be very much in error. Such is indeed found to be the case; the test record is so nonlinear, due to the increased specimen compliance caused by matrix cracking, that the values of P_Q extracted by the data reduction scheme

described above, range from fifty to seventy per cent of the corresponding values of P_{max}. These values of P_Q do correspond to small amounts of material damage, as indicated by the fact that symptoms of matrix cracking were rather sparse at the load P_Q, and became fully developed only at loads significantly higher than P_Q. Of course, the fracture strength is calculated on the basis of damage containment in this laminate, rather than on the basis of actual crack growth. This damage containment approach may seem somewhat inappropriate, since it does not actually characterize the initiation of unstable crack growth. However, because a single continuous crack simply cannot exist in the discrete fiber bundles of the damaged zone, the damage containment approach is the only viable means of characterizing fracture strength in the laminate of interest. It should also be noted that a recognizable crack did form in the undamaged portion of the specimen ligament, and that the formation and initial growth of this crack occurred in the plane of the starter notch.

The failure surfaces of the unidirectional specimens for which α=45° (Figure 13) exhibit none of the indications of extensive material damage discussed above. The crack formed at the tip of the starter notch, and grew as a single crack to the edge of the specimen. However, the path of crack growth was always along a plane parallel to the fibers, in preference to the plane of the starter notch. Because of the asymmetry of the path of crack growth with respect to the applied

load, the crack extended along this path under a mixture of mode I and mode II conditions. With more sophisticated test procedures, these modes could have been decoupled experimentally; however, the available test data was sufficient only for the calculation of a single fracture strength K_Q, of uncertain meaning, for each specimen of this laminate.

The crack also grew along a plane parallel to the fibers in the unidirectional specimens for which α=90° (Figure 14). Of course, such behavior is not at all surprising, as the material, the starter notch, and the loading pattern all favor the observed direction of crack growth. While these specimens are a perfect example of brittle fracture, at least as judged from the appearance of the failure surfaces, their very predictability makes them relatively uninteresting.

A smooth, planar failure surface, aligned with the starter notch, was also developed in the multi-directional specimens with an α of $(0°/\pm45°/90°)_s$. Fractographic examination of the failure surfaces (Figure 15) of these specimens indicates that crack growth occurred on a ply-by-ply basis in a region near the crack tip [28]. However, the region of independent crack growth was very small, extending roughly 0.010 inches from the tip of the starter notch, and the damage accumulated within this region did not induce any noticeable nonlinearity in the data records for these specimens. Moreover, unstable crack growth was initiated by simultaneous failure of all the specimen plies at a point on the boundary of the damage zone in the plane of the starter notch.

As is clearly shown in Figure 15, subsequent crack growth occurred within that same plane.

The failure surfaces of the multi-directional specimens for which $\alpha=(\pm 45°)_s$, shown in Figure 16, are quite interesting in a number of ways. As in the other multi-directional specimens, a region of independent crack growth exists near the tip of the starter notch [28]. The size of this region is about the same in both sets of specimens, so the data records of the $(\pm 45°)_s$ specimens are also quite linear, and the calculated values of K_Q are based on the initiation of unstable crack growth. The unstable crack formed and grew, at least for a short distance, in the plane of the starter notch. Crack growth was not, however, confined to the plane of the starter notch, and the failure surfaces indicate that the running crack eventually switched from its initial plane of growth to one of the two planes of weakness in the material. This phenomenon is obviously dynamic, so an in-depth discussion of it is well beyond the scope of this work. It is interesting to note, though, that the degree to which the path of crack growth is coplanar with the starter notch increases with the length of the starter notch. This observation indicates that, as might be expected on the basis of prior experience with metals, the influence of a crack increases with crack length.

The final question to which the experimental program was addressed

is concerned with the use of metals-based LEFM to characterize the initiation of unstable crack growth in fiber composite laminates. The test results indicate that such an approach is warranted. The reproducibility tests gave satisfactorily consistent results[2], as indicated by the load-displacement curves shown in Figure 17 and 18. The average values of K_Q obtained from the reproducibility tests are

$\alpha = 0°$: $K_Q = 28.8 \times 10^3$ lb/in$^2\sqrt{\text{in}}$ $^{+0.4\%}_{-5.5\%}$

$\alpha = (0°/\pm45°/90°)_s$: $K_Q = 21.7 \times 10^3$ lb/in$^2\sqrt{\text{in}}$ $^{+1.7\%}_{-3.2\%}$

The scatter of these results compares quite well to that encountered in fracture testing of metals. These results, and those shown in Table IV are also fairly consistent with results obtained independently by Halpin [29]

$\alpha = (0°/\pm45°/90°)_s$: $K_Q = 25\text{-}28 \times 10^3$ lb/in$^2\sqrt{\text{in}}$

and Weiss [30]

$\alpha = 0°$: $K_Q = 31 \times 10^3$ lb/in$^2\sqrt{\text{in}}$

$\alpha = (\pm45°)_s$: $K_Q = 19 \times 10^3$ lb/in$^2\sqrt{\text{in}}$

using different specimen configurations and loading arrangements.

---

[2]One exception occurred in the unidirectional specimen set; because this specimen was the first of the entire program to be tested, its anomalous behavior is more likely due to inexperience with the test procedures than to material behavior.

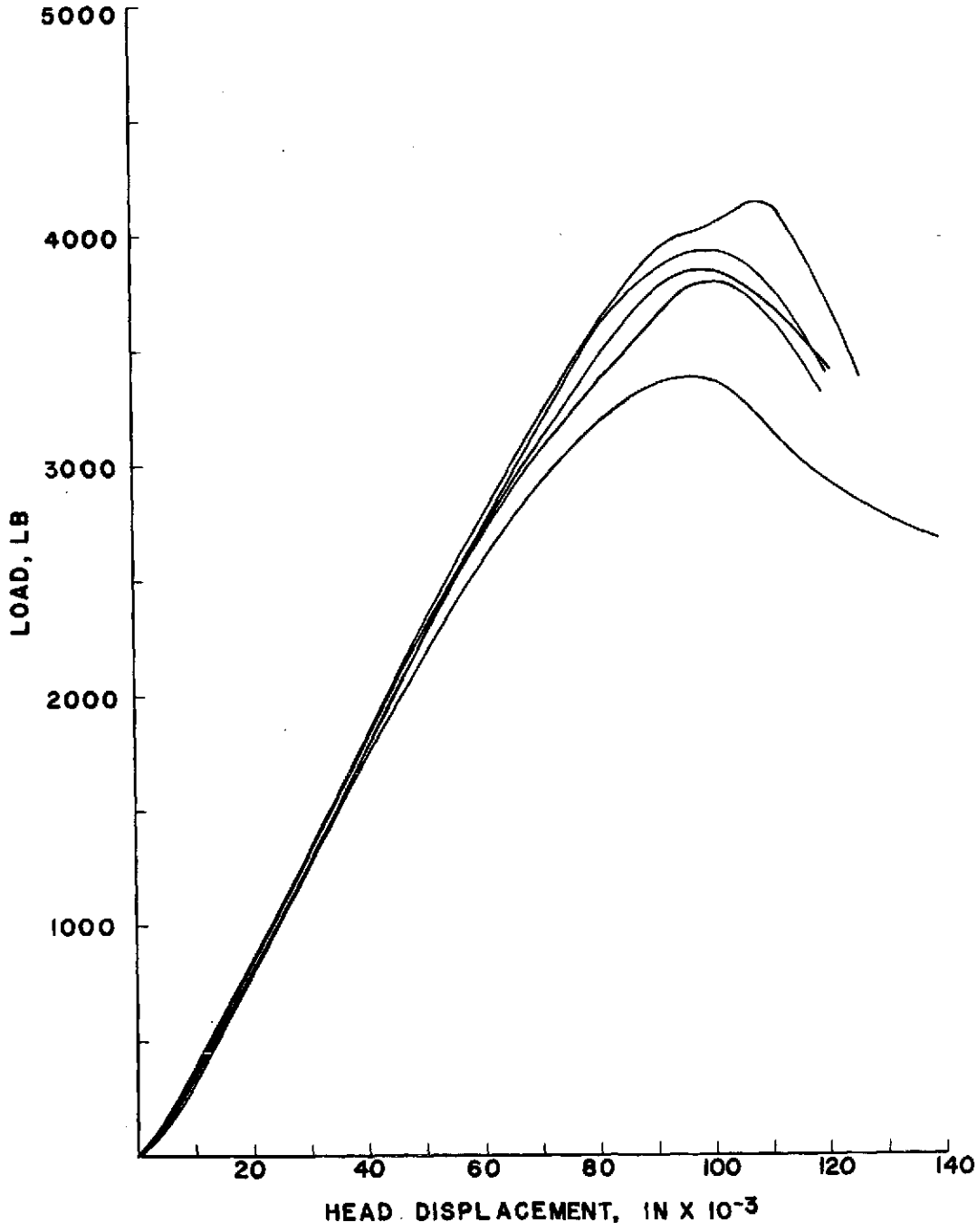

Figure 17. Traces of load vs. cross-head displacement for five specimens of the reproducibility tests for the unidirectional 0° laminate (a = 0.4 inch).

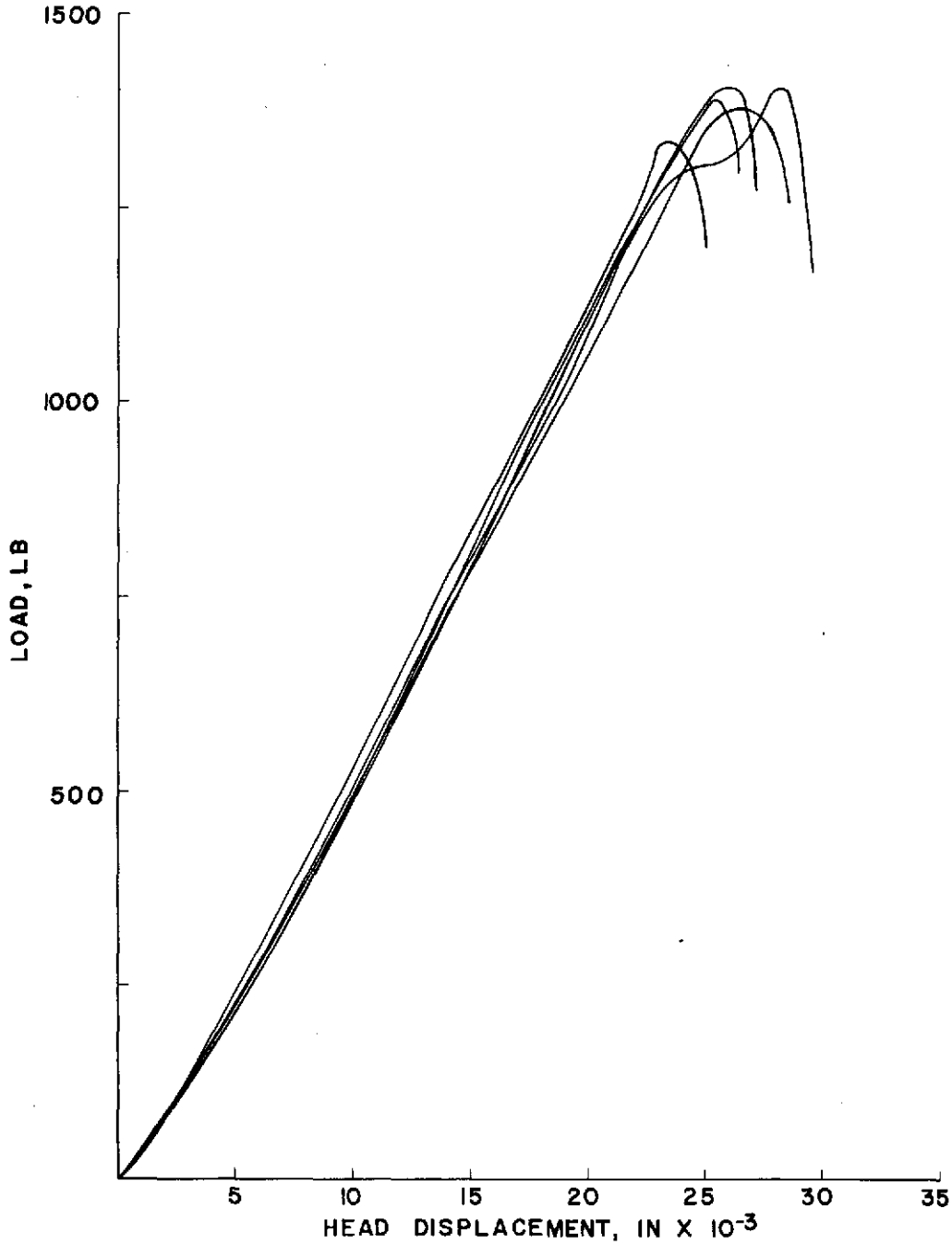

Figure 18. Traces of load vs. cross-head displacement for five specimens of the reproducibility tests for the multi-directional $(0°/\pm45°/90°)_s$ laminate (a = 0.4 inch).

Inspection of Table IV will further show that the values of K_Q obtained for different specimens of a given laminate are within a reasonable range of $\overline{K}_Q$ for that laminate. Most of the larger deviations between K_Q and $\overline{K}_Q$ occurred for the specimens with sub-size starter notches, so the indicated range of the fracture strengths is actually somewhat larger than would be found if the procedures of [25] were followed exactly. However, even the larger deviations are not excessive.

IV.5 Conclusions

The scope of the test program was admittedly quite limited, and any conclusions must therefore be regarded as tentative. Subject to this limitation, however, some conclusions may certainly be drawn. Composite laminates may fail due to unstable growth of a single crack, and this crack may be induced by a pre-existing sharp notch. Moreover, the path of the unstable crack growth is often in the plane of the starter notch, at least during the initial stages of unstable crack growth. Finally, even when the path of crack growth is not at all coplanar with the initial notch, or when material damage prior to unstable crack growth is so extensive as to invalidate the use of a linear elastic specimen model, metals-based LEFM seems to provide a meaningful strength characterization of sharply notched fiber composite laminates.

CHAPTER V

STRAIN ENERGY AND THE FRACTURE PROCESS

V.1 Introduction

In many instances, the concept of fracture strength is a perfectly adequate characterization of the initation of crack growth in a given material. However, when mixed mode conditions exist, fracture strength is a somewhat less satisfactory representation of material behavior, as is noted in discussion of the unidirectional 45° specimens (see chapter IV). Although a single fracture strength can be calculated for these specimens, and is apparently representative of the specimen behavior (Table IV), the result is not really general, even if stated in terms of K_{IQ} and K_{IIQ}, the mode I and mode II components of fracture strength. In fact, both K_{IQ} and K_{IIQ} vary, by definition, as the relative amounts of the two modes of crack behavior change. Thus, since the interaction between modes is not yet known, the results obtained from a given mixed mode fracture test cannot be used to predict unstable crack growth under different mixed mode conditions. Clearly then, the concept of fracture strength alone is of little use for characterizing mixed mode crack growth.

An alternative to the fracture strength approach to the characterization of initial crack growth may be developed by considering a loaded cracked elastic body as a thermodynamic system. Application of the first law of thermodynamics to this system leads to the

conclusion that the existing crack will grow only if the energy of the body undergoes no net change as a result of such crack growth [31]. This statement, in turn, implies the existence of one or more energy sources and one or more energy sinks associated with the process of crack growth.

The energy source for the process of crack growth is simply the recoverable elastic energy within the body, which necessarily decreases from some initial value as crack length increases. Although this energy source is conceptually the same in all cases, the calculation of its magnitude varies according to the boundary conditions used to introduce load into the body. In the case of fixed displacement boundary conditions, the increase in the compliance of the body due to crack growth results in a decrease in the elastic energy in the body; the amount of energy thus released by some increment in the crack length is the energy source for that crack extension. In the case of fixed traction loading, the boundaries of the body undergo displacements as a result of the increase in the compliance of the body accompanying crack growth. The applied tractions act through these boundary displacements, thus performing work on the body. It may be shown that half of this work is stored as strain energy in the body, the remainder being the source of energy for crack growth [32].

Clearly, the manner of calculating the energy source for crack growth varies with the type of loading conditions considered. However,

since the single energy source of interest is a function of only the state of stress within the body, it is not surprising that the two analytical approaches described above lead to an expression for the magnitude of the energy source which is the same function of stress components and material properties for either type of boundary conditions [32]. As the type of boundary conditions is immaterial to the result, the simpler case of fixed boundary displacements is usually considered for calculating the magnitude of the energy source for crack growth. Such calculations yield an expression for the rate at which the strain energy of the body changes with respect to crack length. Thus stated, the energy source for crack growth is the strain energy release rate, denoted by G.

The energy sinks associated with crack growth are less well defined than the energy source. The possible presence of a number of dissipative mechanisms during the crack growth process has been noted, but few of these mechanisms have been quantitatively treated. However, most of these energy sinks are known to be material parameters. This single element of information assumes great significance in view of the statement that crack growth will occur only if the magnitudes of the energy source and the energy sinks are equal.

It follows from the material dependent nature of the energy sinks that some specific value of G, the energy source, is characteristic of crack growth in a given material (cf. stress intensity factor and

fracture strength). The particular advantage of this energy characterization of crack instability is that, as shown below, it does represent the interaction between modes.

V.2 Analysis

The application of an energy criterion of crack growth to fiber composite laminates requires the development of an expression for G in an anisotropic material. This calculation may be based on the situation shown schematically in Figure 19; a crack in the same remotely loaded, unbounded, anisotropic plane defined in chapter II extends by some small amount δ. Because the material is elastic, the strain energy released by this process is exactly equal to the work required to return the crack to its original configuration by closing up the incremental crack extension. But then, in the limit as δ approaches zero, the amount of work required for crack closure per unit length of crack extension is simply equal to G.

If the crack extension is collinear with the original crack, as shown in Figure 19, the amount of work required to close up the crack extension is easily calculated, as the necessary tractions and displacements are known from the results obtained in chapter II. The calculation of G is then a conceptually straightforward exercise, though the details are quite tedious, particularly for the case of mixed mode behavior in the crack-tip region. These details are

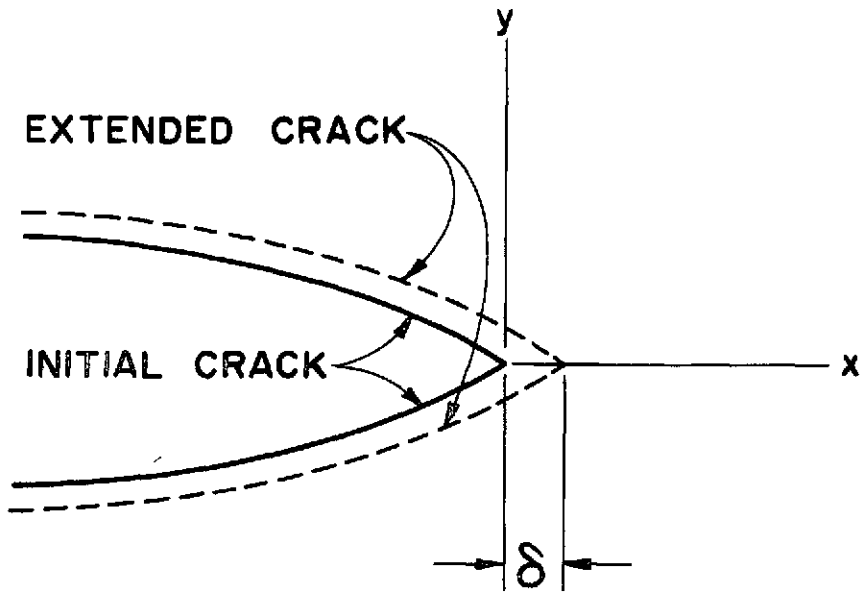

Figure 19. Schematic representation of the crack growth model used to calculate the strain energy release rate. Note that the boundaries of the initial and extended cracks are geometrically similar.

discussed elsewhere [26] and need not be repeated in this work, it being sufficient to note the resulting expression for the strain energy release rate in the case of mixed mode crack behavior.

$$G = -(K_I/2)\beta_{22}\, Im\{[K_I(\mu_1+\mu_2) + K_{II}]/\mu_1\mu_2\} + (K_{II}/2)\beta_{11}\, Im\{K_I\mu_1\mu_2 + K_{II}(\mu_1+\mu_2)\} \quad (60)$$

The interaction between modes I and II is clearly apparent in those terms of (60) which contain the product $K_I K_{II}$. While, in the case of pure single mode behavior, (60) reduces to the appropriate expression for G_I or G_{II}, it it noted that the strain energy release rate for mixed mode behavior is not simply the sum of G_I and G_{II}. Thus, in contrast to the case in isotropic materials, two modes of crack behavior do interact in a non-trivial manner in anisotropic media.

V.3 Calculations

A value of G_Q, the candidate strain energy release rate at the onset of crack growth in a material may be obtained by evaluating (60) using K_{IQ} and K_{IIQ}, the components of the fracture strength for that material. Such calculations were performed for each of the specimens of the experimental program discussed in chapter IV. Except in the case of the specimens of the unidirectional 45° laminate, this

calculation of G_Q was greatly simplified by the observation that, because the materials, load, and specimen geometry are symmetric relative to the crack, only mode I behavior exists in the specimen. Thus, in these cases, K_{IQ} is simply the fracture strength of the specimen, K_{IIQ} is zero, and (60) reduces to the mode I strain energy release rate.

The calculation of G_Q for specimens of the unidirectional 45° laminate is somewhat more complex, as both mode I and mode II behavior exist in these specimens. Thus, neither K_{IQ} nor K_{IIQ} is zero, nor is either component of the fracture strength explicitly known. As noted in chapter IV, K_{IQ} and K_{IIQ} cannot be directly evaluated from available test data; an alternative procedure must therefore be employed.

The procedure chosen to calculate K_{IQ} and K_{IIQ} was a numerical analysis based on a finite element simulation of the laboratory tests. The specimen geometry was modelled by a two-dimensional grid of linear displacement triangular elements; the lamination theory material model of the test laminate was again employed. The boundary conditions for the finite element model were chosen to correspond to those for the actual laboratory specimens at the initiation of crack growth, as denoted by P_Q. The solution of this 714 degree-of-freedom problem required approximately two minutes on the Univac 1108.

In order to extract K_{IQ} and K_{IIQ} from the numerical data, expressions

for the combined mode I and mode II stress fields in the crack-tip region were obtained simply by adding (41a-c) and 48(a-c). When evaluated on the crack-axis ($\theta = 0°$), the mode I and mode II components of this combined stress field have the simple forms

$$\sigma_y(r,0°) = K_I/\sqrt{2\pi r} \tag{61a}$$

$$\tau_{xy}(r,0°) = K_{II}/\sqrt{2\pi r} \tag{61b}$$

Taking the logarithm of these stress expressions yields the result

$$\log [\sigma_y(r,0°)] = \log [K_I/\sqrt{2\pi}] - \frac{1}{2} \log [r] \tag{62a}$$

$$\log [\tau_{xy}(r,0°)] = \log [K_{II}/\sqrt{2\pi}] - \frac{1}{2} \log [r] \tag{62b}$$

The desired method for determining K_I and K_{II} is based on the linear form of (62a-b). Values of $\sigma_y(r,0°)$ and $\tau_{xy}(r,0°)$ are obtained from the numerical analysis, and plotted against r on a logarithmic scale (Figure 20). Straight lines having a slope of -1/2 are then fitted to these data[1], and the values of K_I and K_{II} obtained by evaluating (62a-b) at any convenient points on those lines. However, since the numerical results simulate the state of the specimen at incipient

[1] The poor fit of these lines to the data shown in Figure 20 is attributed to the use of a crude finite element grid for a bending problem. However, finite element results for those specimens exhibiting only mode I behavior indicate that the data point closest to the crack-tip is accurate.

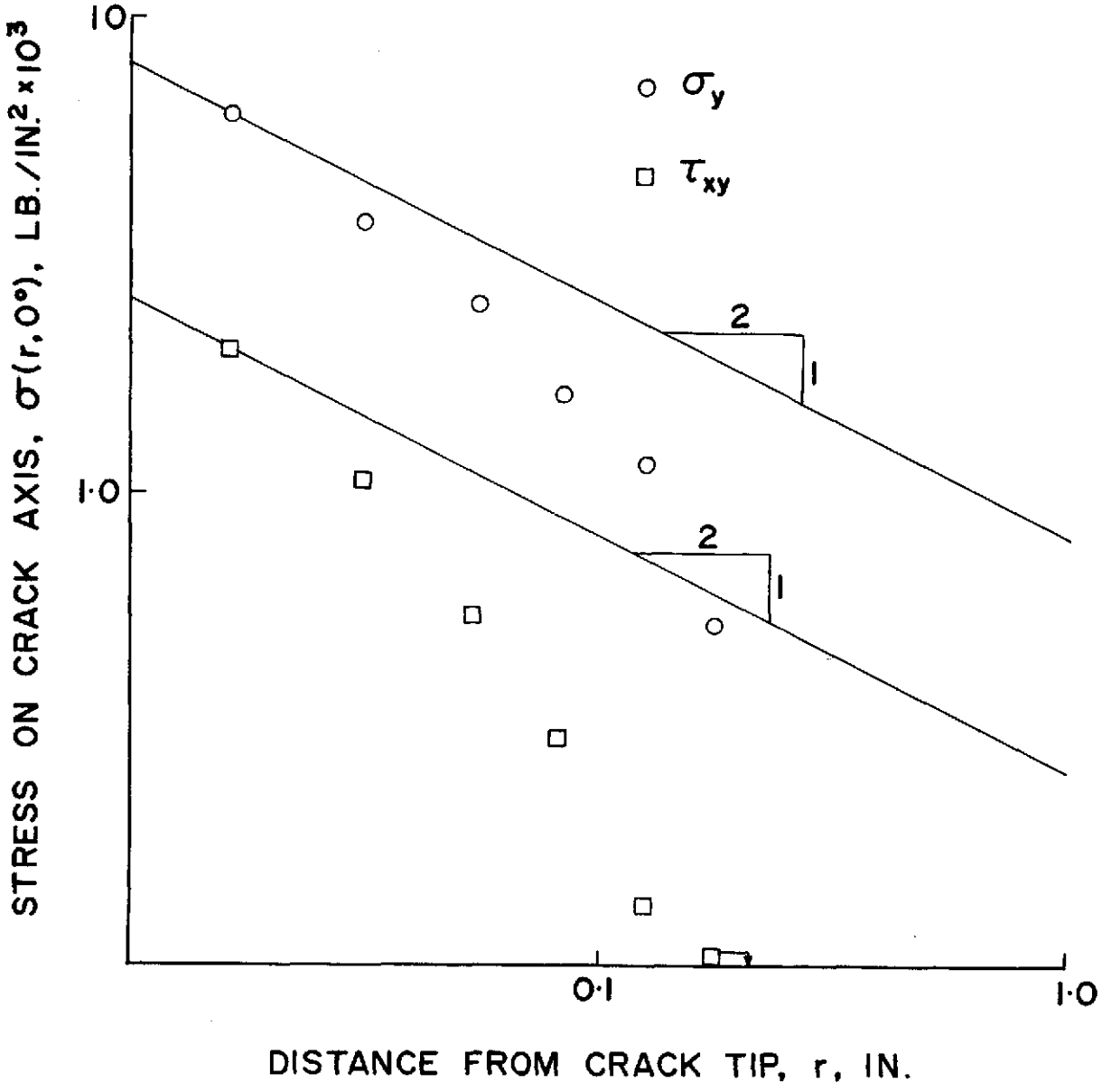

Figure 20. Graphical procedure for decoupling K_{IQ} and K_{IIQ} in the mixed mode unidirectional 45° specimens.

crack growth, the values thus obtained for K_I and K_{II} are actually the mode I and mode II components of the fracture strength, K_{IQ} and K_{IIQ}. With these values known, the calculation of G_Q for the unidirectional 45° specimens is a simple algebraic exercise.

This same result may be obtained in a somewhat less complicated fashion by evaluating J, Rice's J-integral [33]. The J-integral has the form

$$J = \int_{\Gamma} \{w\,dy - \underset{\sim}{T} \cdot \partial \underset{\sim}{u}/\partial x\, ds\} \tag{63}$$

where Γ is a continuous path around the crack tip, w is the strain energy density, (x,y) are coordinate directions, $\underset{\sim}{T}$ is the traction vector on Γ, $\underset{\sim}{u}$ is the displacement vector on Γ, and ds is a positively directed segment of Γ (Figure 21). The value of J was determined numerically, by implementing the technique suggested in [34] in the finite element analysis described above. The values of J thus obtained are denoted J_Q, the subscript Q indicating the state of a specimen at the initation of crack growth. As implied above, J_Q and G_Q are exactly equivalent for an elastic material.

It should be noted that (60) is a valid expression for the strain energy release rate only if the path of crack growth is at least initially collinear with the existing crack. Moreover, the equivalence of J_Q and G_Q is dependent upon this same condition. Thus, for the unidirectional 45° specimens – in which the path of crack growth is not at all collinear with the starter notch – the values obtained for G_Q and J_Q are not strictly valid strain energy release rates for

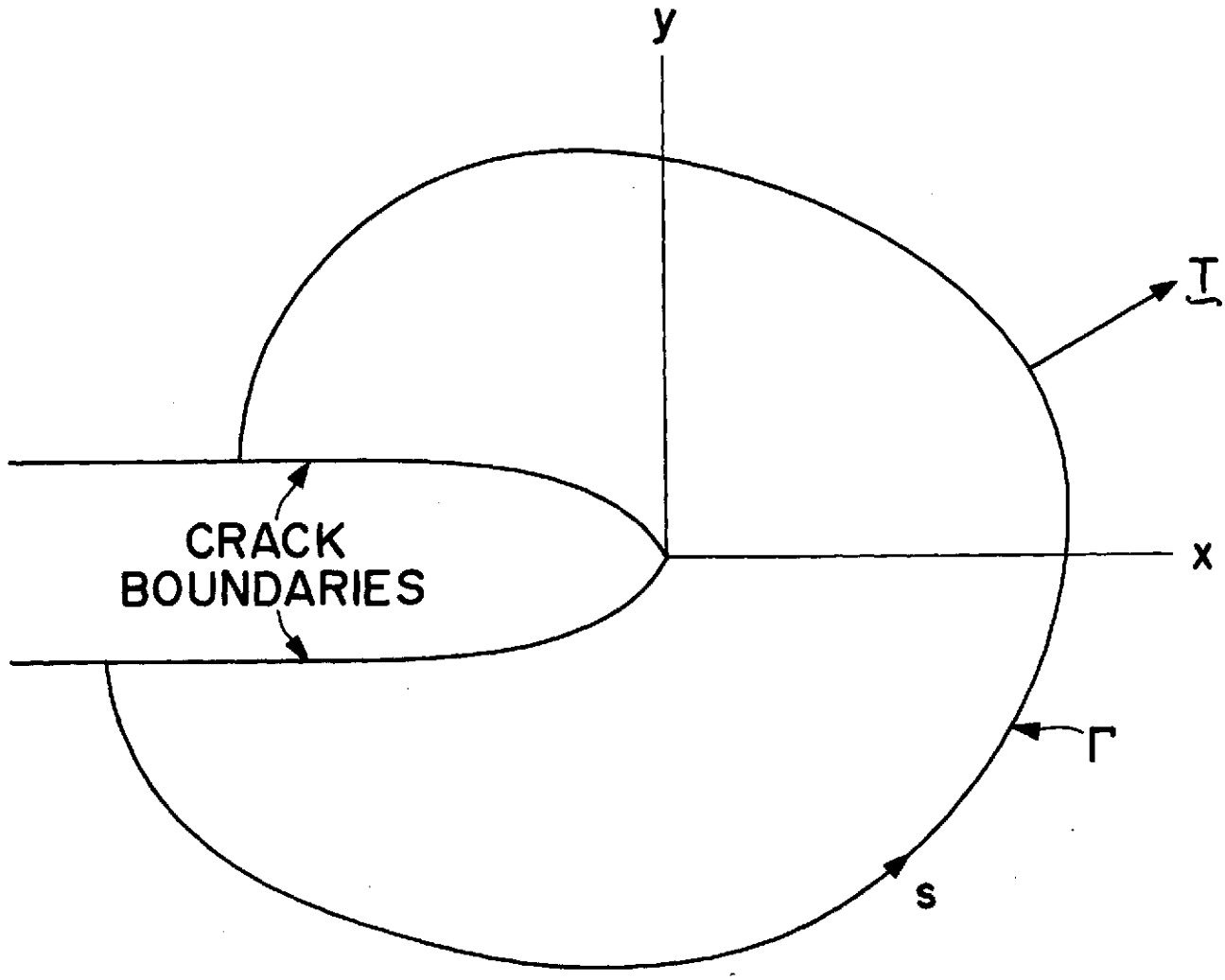

Figure 21. Coordinate system and integration path for calculating Rice's J-integral.

incipient crack growth. Such values were nevertheless calculated, simply because no viable alternative means of determining the desired strain energy release rate were available.

V.4 Results and discussion

The procedures described above were used to calculate values of G_Q and J_Q for each of the specimens successfully tested in the experimental program. These values are shown, in cross-plotted form, in Figure 22.

It is seen in Figure 22 that the energy parameter data fall into two distinct groups, separated by approximately two orders of magnitude. The segregation of these data into two distinct and widely separated groups indicates that the data are characterizing two distinct phenomena. This indication may be confirmed, and the phenomena in question identified, by further investigation of the energy data groups.

The low energy group is particularly interesting because of the significant differences in behavior exhibited by specimens of the two unidirectional laminates which comprise this group. The specimens of the 90° laminate displayed only mode I response, and a path of crack growth which is completely collinear with the starter notch. This behavior contrasts markedly, of course, with that exhibited by the specimens of the 45° laminate, in which both mode I and mode II

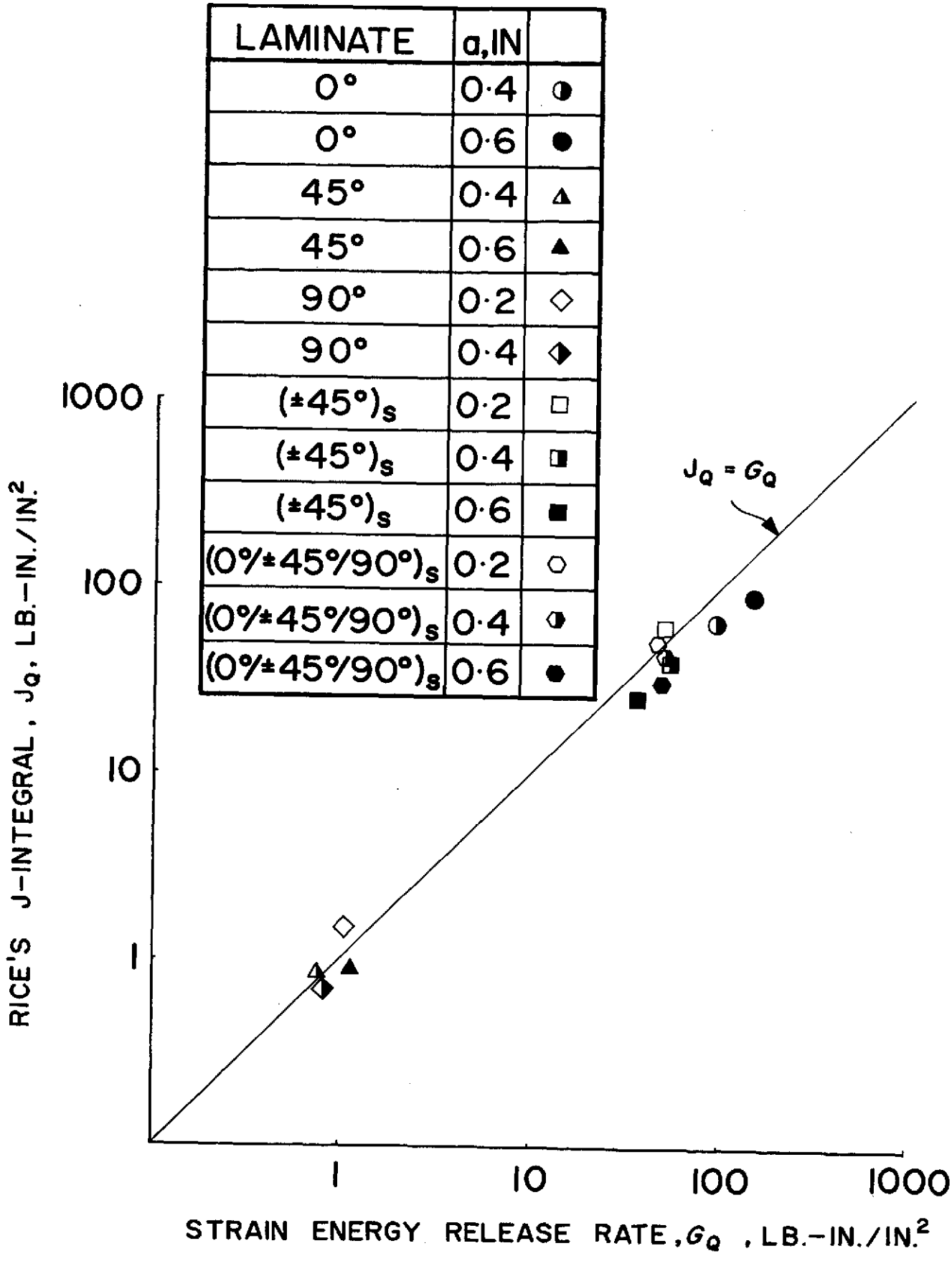

Figure 22. Plot of J_Q, Rice's J-integral, vs. G_Q, the strain energy release rate. Note that the data are segregated into two distinct, widely separated groups.

effects were present, as well as a path of crack growth which is not at all collinear with the starter notch. The fact that these very different types of behavior are characterized by roughly the same value of G_Q is attributed to the one point common to all the specimens of the low energy group — in all specimens of this group the crack propagated entirely between fibers, either within the matrix or along the fiber-matrix interface. It thus seems that the low energy data group corresponds to the phenomenon of crack growth without fiber breakage.

The phenomenon of matrix fracture may be further characterized in terms of the hoop, or tensile stress, along the actual path of crack growth. Values of this stress component were obtained from the finite element analyses described above, for specimens of both laminates of the low energy group. A comparison of the hoop stresses along the fracture paths is shown in Figure 23. Clearly, matrix fracture is initiated by the same tensile stress field in both laminates, from which it may be tentatively concluded that matrix fracture in general is governed by the tensile stress normal to the fibers.

The interpretation of the low energy data group as the result of crack growth without fiber breakage suggests that the high energy data group corresponds to crack growth with fiber breakage. This interpretation of the high energy group is supported by the physical behavior of the specimens within this group.

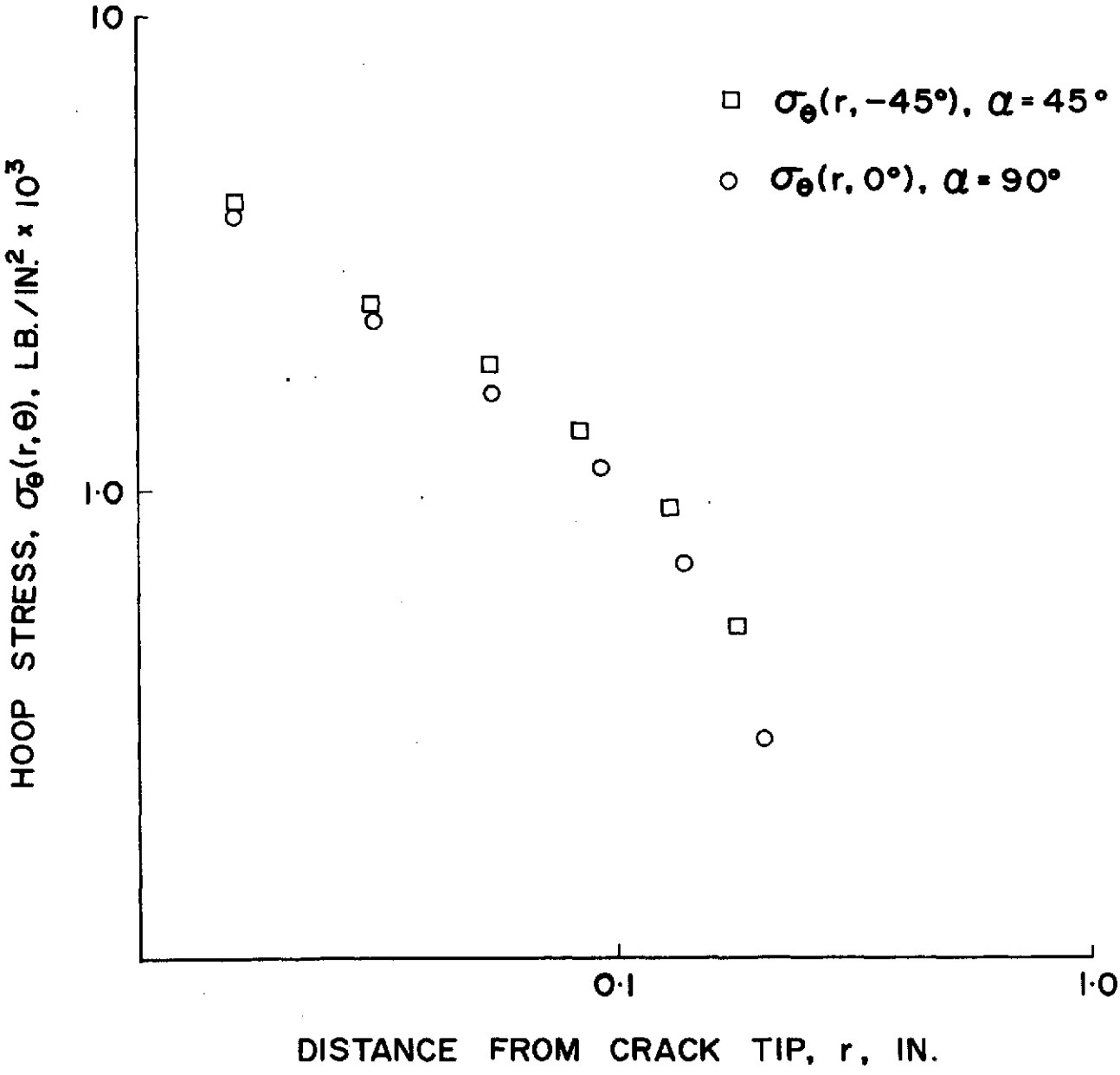

Figure 23. Hoop stresses on the fracture paths for laminates of the low energy group.

V.5 Conclusions

The strain energy release rate seems to be a valid approach to characterizing initial crack instability in a composite laminate, even when the physical behavior of the crack does not precisely conform to the basic assumption of collinear crack growth. In cases involving mixed mode behavior, the strain energy release rate is a particularly useful concept, as it can characterize the interaction between modes.

The values of G_Q obtained for the specimens of the test program suggest that crack growth in a composite laminate may be typified according to whether or not the growing crack broke fibers. In the latter case, the initation of crack growth is apparently governed by the tensile stress on the actual path of crack propagation; as is shown in chapter VI, the initation of crack growth with fiber breakage may be related to the tensile strength of the laminate plies parallel to the fiber direction.

CHAPTER VI

PREDICTION OF FRACTURE STRENGTHS OF FIBER COMPOSITE LAMINATES

VI.1 Introduction

The work discussed in the preceding chapters indicates that the procedures of metals-based LEFM, suitably modified for anisotropy, may be meaningfully applied to the study of crack extension in a graphite/epoxy composite laminate. In particular, the initiation of crack growth in such a laminate may be characterized by a fracture strength, a material property of that laminate. However, different laminates of a single fiber/matrix system, such as those considered in this work, are not truly unique materials; for example, the elastic properties of an arbitrary laminate may be stated as a function of the elastic properties of the basic material ply, and the orientation of those plies within the laminate [16]. It is therefore postulated that the fracture strength of a given composite laminate may likewise be a function of the fracture properties of the individual ply, and the relative orientation of those plies.

An analytical model to predict the fracture strength of specially orthotropic laminates as a function of ply properties and ply orientation is developed in this chapter. The model is based on the assumption that crack growth occurs in a laminate when the ply stresses within the crack-tip region reach the same level as that attained at the initiation of crack growth in a unidirectional material.

VI.2 Analysis

The analytical model for the prediction of fracture strength is based on the stress analysis of a cracked, anisotropic, homogeneous body (see chapter II), combined with the equations of lamination theory [16] to provide an estimate of the stresses in each ply of the laminate. As noted previously, the use of this homogeneous material model precludes any consideration of microstructural phenomena such as fiber-matrix interactions, fiber buckling, debonding, etc. in the actual course of the analysis. However, the results of the analysis do provide some estimates about the relative importance of these microstructural effects.

The general laminate to be considered consists of k angle-ply components, arranged symmetrically with respect to the global x-y coordinate system, and is mid-plane symmetric. In terms of the ply-angle α (Figure 24), this laminate may be described by

$$\alpha = (\pm\phi_{1\lambda_1}/\pm\phi_{2\lambda_2}/\cdots/\pm\phi_{i\lambda_i}/\cdots\pm\phi_{k\lambda_k})_s \qquad (64)$$

where ϕ_i is the orientation of the i^{th} angle-ply component of the laminate, and λ_i is the relative thickness of that component. In the global coordinate system, this laminate is specially orthotropic. The crack is taken to be oriented along the x-axis (Figure 24) and subjected to mode I loading. The results of the experimental program (see chapter IV) show that, under the specified conditions, the path of initial crack growth is in the plane of the existing crack.

On this observed path of crack growth, within the crack-tip

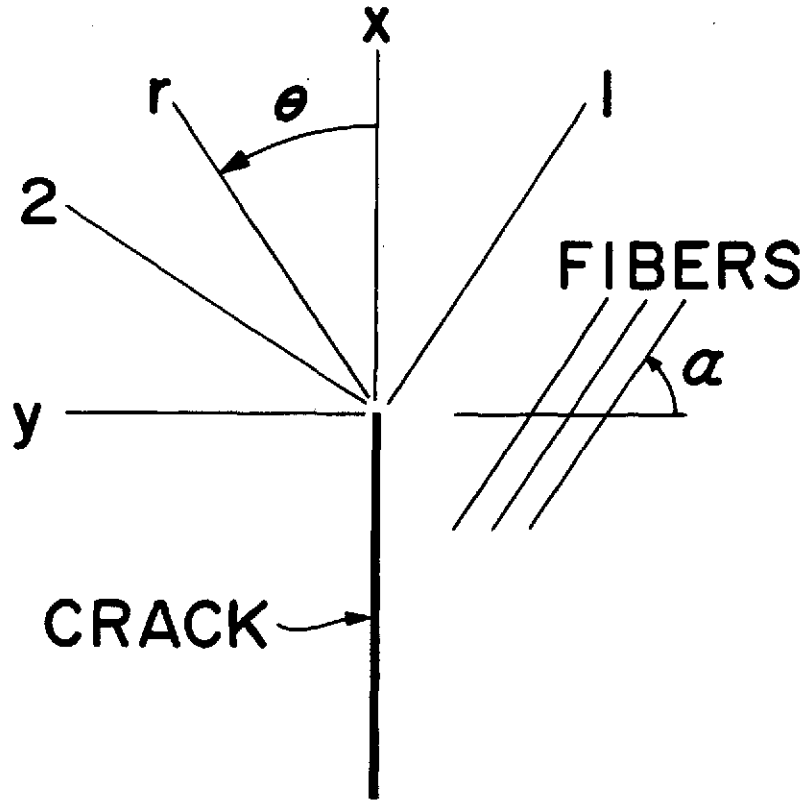

Figure 24. Crack-tip coordinate systems in a fiber composite ply. The global coordinate systems, (x,y) and (r,θ), are fixed relative to the crack, and thus do not vary from ply to ply. The material coordinate system is determined by α, the ply orientation angle.

region, the stresses given by (41a-c) have the form

$$\begin{Bmatrix} \sigma_x \\ \sigma_y \\ \tau_{xy} \end{Bmatrix} = K_I/\sqrt{2\pi r} \begin{Bmatrix} -Re\{\mu_1\mu_2\} \\ 1 \\ 0 \end{Bmatrix} \tag{65}$$

where K_I is the mode I stress intensity factor, r is the distance from the crack tip, and μ_1,μ_2 are the distinct roots of (3). In the particularly simple case of a specially orthotropic laminate, (3) is reduced to a bi-quadratic equation, and it is easily shown that

$$-Re\{\mu_1\mu_2\} = \sqrt{\beta_{22}/\beta_{11}} \tag{66}$$

where β_{mn} are the global compliances of the material.

The basic assumption of lamination theory is that the global strains at a point are identical through the thickness of the laminate. Thus, the global strains in the i^{th} ply are easily obtained in terms of the laminate stresses (65)

$$\begin{Bmatrix} \varepsilon_x \\ \varepsilon_y \\ \gamma_{xy} \end{Bmatrix}_i = K_I/\sqrt{2\pi r}\,[\beta_{mn}] \begin{Bmatrix} \sqrt{\beta_{22}/\beta_{11}} \\ 1 \\ 0 \end{Bmatrix} \tag{67}$$

The global stresses in the i^{th} ply may now be calculated from (67) using $[\overline{Q}_{mn}]_i$, the stiffness matrix of the i^{th} laminate in the

global coordinate system,

$$\begin{Bmatrix} \sigma_x \\ \sigma_y \\ \tau_{xy} \end{Bmatrix}_i = K_I/\sqrt{2\pi r}\ [\bar{Q}_{mn}]_i\ [\beta_{mn}] \begin{Bmatrix} \sqrt{\beta_{22}/\beta_{11}} \\ 1 \\ 0 \end{Bmatrix} \tag{68}$$

Finally, the principal stresses[1] in the i^{th} ply may be obtained by a tensor transformation of the global stresses in that ply

$$\begin{Bmatrix} \sigma_1 \\ \sigma_2 \\ \tau_{12} \end{Bmatrix}_i = K_I/\sqrt{2\pi r}\ [T_{mn}]_i\ [\bar{Q}_{mn}]_i [\beta_{mn}] \begin{Bmatrix} \sqrt{\beta_{22}/\beta_{11}} \\ 1 \\ 0 \end{Bmatrix} \tag{69}$$

where $[T_{mn}]_i$ is a second order tensor transformation [1] for the i^{th} ply. As i is varied from 1 to 2k, (69) gives the principal stress field within the crack-tip region of each ply of the laminate. The form of (69) may be simplified by denoting the matrix products on the right hand size of (69) by the vector $\{\xi\}_i$ such that

$$\begin{Bmatrix} \sigma_1 \\ \sigma_2 \\ \tau_{12} \end{Bmatrix}_i = K_I/\sqrt{2\pi r} \begin{Bmatrix} \xi_1 \\ \xi_2 \\ \xi_3 \end{Bmatrix}_i \tag{70}$$

The vector $\{\xi\}_i$ is a function of ply properties and orientations, and is therefore known for each ply of a given laminate.

[1] The 1- and 2-directions (parallel and transverse to the fibers, respectively, as shown in Figure 24) are conventionally referred to as principal directions of an orthotropic fiber composite ply.

VI.3 Fracture criteria

In chapter V, it is noted that the data from the experimental program may be grouped according to the orientation of the path of crack growth relative to the material. On the basis of this observation, two criteria may be posited for the initiation of crack growth in the i^{th} ply. The first criterion corresponds to the case of crack growth parallel to material fibers, an event termed matrix fracture; the second criterion corresponds to the case of crack growth across fibers, an event termed fiber fracture. Fiber fracture is assumed to initiate when σ_1 achieves some critical condition; a separate critical condition, when achieved by σ_2, indicates the initation of matrix fracture.

The critical conditions for fiber fracture and matrix fracture are based on the singular nature of (70). Because of this stress singularity, it is evident that there exist two distances, r_f and r_m, such that

$$\sigma_1(r, 0°) \geq \sigma_{1u} \qquad r \leq r_f \tag{71a}$$

$$\sigma_2(r, 0°) \geq \sigma_{2u} \qquad r \leq r_m \tag{71b}$$

where σ_{1u} and σ_{2u} are the principal strengths of a material ply. The limiting cases of (71a-b)

$$\sigma_1(r_f, 0°) = \sigma_{1u} \tag{72a}$$

$$\sigma_2(r_m, 0°) = \sigma_{2u} \tag{72b}$$

are simply the criteria for incipient fiber and matrix fracture, respectively, in any ply of a laminate.

In order to use (72a-b) as fracture criteria, it is necessary to determine r_f and r_m. These values may be calculated from (70), (72a-b), and the experimental data discussed in chapter IV.[2] The evaluation of r_f is based on the experimentally determined fracture strength of the unidirectional 0° laminate, denoted by K_Q^0. Combining this value with the expression for σ_1 obtained by evaluating (70) for the 0° laminate yields

$$\sigma_1 = K_Q^0/\sqrt{2\pi r} \quad . \tag{73}$$

The value of r_f is then obtained simply by combining (73) with (72a)

$$r_f = (K_Q^0/\sigma_{1u})^2/2\pi \tag{74}$$

A similar procedure, using K_Q^{90}, the fracture strength of the 90° laminate, yields an expression for r_m

$$r_m = (K_Q^{90}/\sigma_{2u})^2/2\pi \tag{75}$$

The physical values of r_f and r_m are easily obtained by substituting the known values of fracture strength and principal material strength

---

[2] Also required for this calculation are the principal elastic properties of a graphite/epoxy material (Table II) and the principal ultimate strengths

$$\sigma_{1u} = 151. \times 10^3 \text{ lb/in}^2$$

$$\sigma_{2u} = 7.7 \times 10^3 \text{ lb/in}^2$$

into (74) and (75). The resulting values of r_f and r_m are found to be

$$r_f = 0.0074 \text{ in.} \tag{76a}$$

$$r_m = 0.0065 \text{ in.} \tag{76b}$$

The distances r_f and r_m are discussed further below, but will be used here as a convenient means of data reduction, with no particular physical significance.

In the i^{th} ply of a laminate, (70) may now be used to compute two values of K_I, corresponding to the initiation of fiber fracture and matrix fracture in that ply. The former value, denoted K_{If}, is obtained by the appropriate substitution of σ_{1u} and r_f into (70), which yields

$$(K_{If})_i = \sigma_{1u}\sqrt{2\pi r_f} \,/\, (\xi_1)_i \tag{77}$$

The initiation of matrix fracture in the i^{th} ply is characterized by the value K_{Im}, obtained by substituting σ_{2u} and r_m into (70)

$$(K_{Im})_i = \sigma_{2u}\sqrt{2\pi r_m} \,/\, (\xi_2)_i \tag{78}$$

For convenience, (77) and (78) may be normalized by (74) to yield

$$(K_{If})_i \,/\, K_Q^0 = 1 \,/\, (\xi_1)_i \tag{79a}$$

$$(K_{Im})_i \,/\, K_Q^0 = (K_Q^{90}/K_Q^0) \,/\, (\xi_2)_i \tag{79b}$$

It is seen that the analytical criteria for fiber and matrix fracture

in the i^{th} ply of a laminate are functions only of the ply orientation, the principal elastic constants of the material system, and two independent fracture strengths. The distances r_f and r_m do not appear in the normalized fracture criteria.

VI.4 Application of the analytical criteria

The simplest class of specially orthotropic fiber composites is the group consisting of single angle-ply laminates. This class corresponds to the general laminate specified by (74) with k = 1, i.e.,

$$\alpha = (\pm\phi)_s \tag{80}$$

The ply orientation angle α varies from 0° to 90°, so this family includes the experimental laminates for which α = 0°, $(\pm 45°)_s$, and 90°. The application of (79a-b) to these laminates is particularly simple, as ξ_1 and ξ_2 have the same values in both plies of the laminate. Thus, single values of K_{If} and K_{Im} characterize fiber and matrix fracture in the entire laminate. These values of K_{If} and K_{Im} were obtained for angle-ply laminates of the graphite/epoxy material specified in Table II. The results of these calculations, in the normalized form obtained from (79a-b), are plotted as a function of ϕ in Figure 25.

The experimental results for the three angle-ply laminates of the test program are also shown, normalized on K_Q^0, in Figure 25. The fact that the results for the two unidirectional laminates fall on the predicted curves is a consequence of the normalized form of

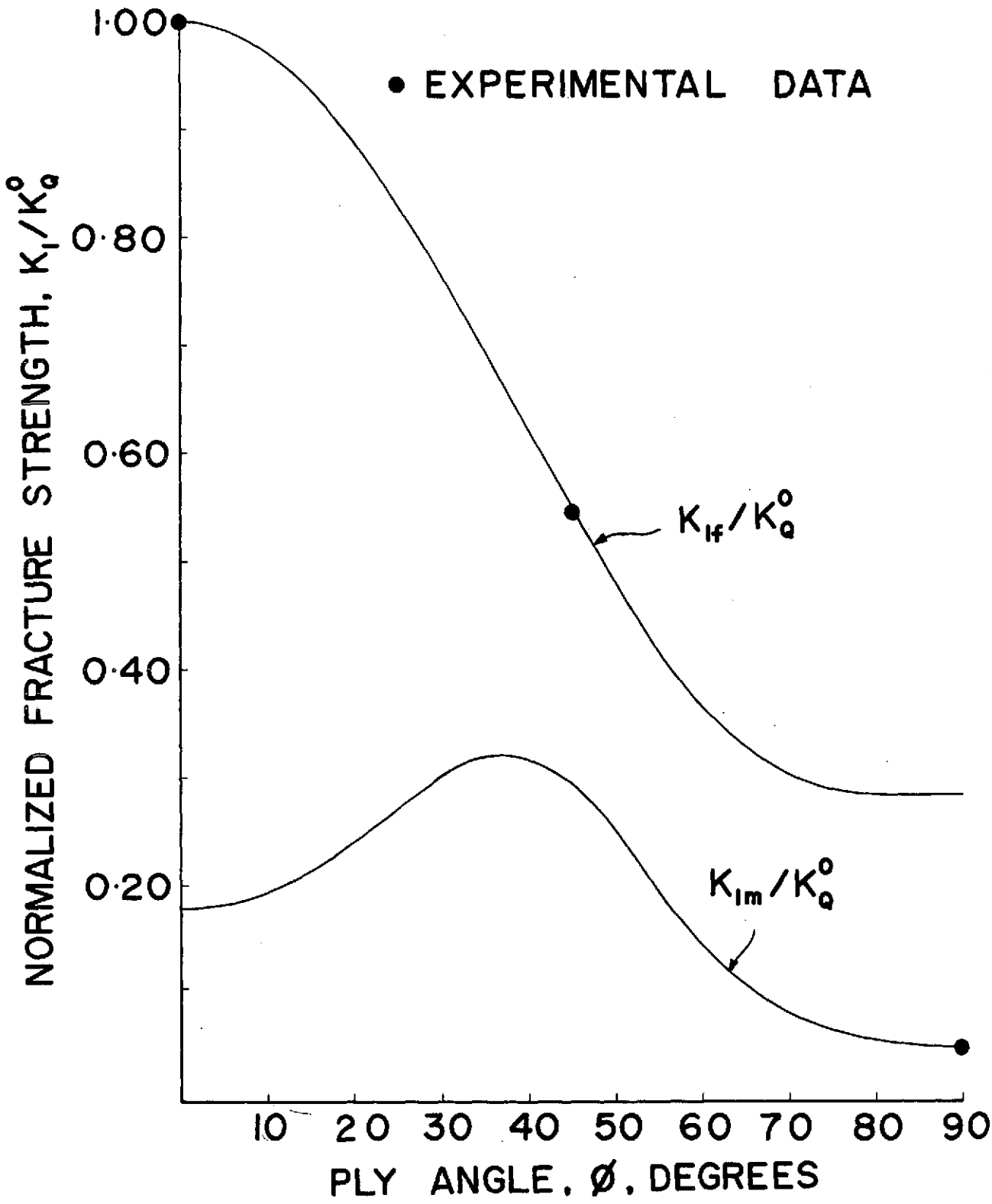

Figure 25. Predicted and experimental fracture strengths of angle-ply graphite/epoxy laminates.

(79a-b). It is however, significant that the result for the $(\pm 45°)_s$ laminate also falls on a predicted curve, namely the curve indicative of fiber fracture. As the crack did grow by breaking fibers in this laminate (see chapter IV), the agreement between the experimental result and the predicted value of K_{If} is very encouraging.

An interesting feature of the analytical model is that two fracture strength curves are obtained, one predicated on fiber fracture and one predicated on matrix fracture. The presence of experimental data on both predicted curves suggests that neither curve describes the behavior of angle-ply laminates for all values of ϕ, and that the actual material behavior must pass from one curve to the other. Theoretically, the transition occurs exactly at $\phi = 90°$, as any lesser value of ϕ implies that there is no possible path of crack growth parallel to all of the fibers. Under such circumstances, crack growth must occur by fiber fracture, and should therefore be characterized by K_{If}. Of course, the transition between fiber fracture and matrix fracture is probably less abrupt and more complex in a real material. However, because the nature of the theoretical transition is so abrupt, it is assumed that the transition phenomenon in real materials does occur quite rapidly, and only for values of ϕ very nearly equal to 90°. Such values of ϕ are not found in engineering applications of fiber composites, so the practical use of the analytical model need not be impeded by the obscure nature of the transition phenomenon.

As noted above, the application of the analytical model to a single angle-ply laminate is particularly straightforward, as the behavior of the entire laminate is characterized by single values of K_{If} and K_{Im}. The problem is significantly more complex for laminates consisting of several angle-ply components, as each component has associated with it single values of K_{If} and K_{Im}. While the choice between K_{If} and K_{Im} for a given angle-ply component may be made on the basis of the above discussion, the question of predicting a fracture strength for the entire laminate is not thus resolved.

A very simple method for predicting the fracture strength of a multi-component specially orthotropic laminate is based on the assumption that the initiation of fiber fracture in any of the angle-ply components corresponds to the initiation of crack growth in the entire laminate. Thus, the angle-ply component for which $\phi_i = 90°$ is completely ignored, as fiber fracture cannot occur in this component; the lowest value of K_{If} for the remaining components is taken to be the fracture strength of the entire laminate.

The first fiber fracture approach may be illustrated by considering the multi-component test laminate for which $\alpha = (0°/\pm 45°/90°)_s$ This laminate has three angle-ply components: twenty-five per cent at $\pm 0°$; fifty per cent at $\pm 45°$; and twenty-five per cent at $\pm 90°$. For each of these components, values of K_{If} and K_{Im} may be obtained

from (79a-b). These values are:

α	K_{If}/K_Q^0	K_{Im}/K_Q^0
±0	0.548	0.274
±45°	0.548	0.274
±90°	0.548	0.274

It is noted that the characterization of the entire laminate by single values of K_{If} and K_{Im} is a consequence of the quasi-isotropic nature of this particular laminate. In general, each angle-ply component of a laminate is characterized by unique values of K_{If} and K_{Im}.

The fracture strength of the laminate in question is predicted to be 0.548 K_Q^0, on the basis of the first instance of fiber fracture in a fiber-dominated angle-ply component. The experimentally determined fracture strength of this laminate (chapter IV) is found to be 0.635 K_Q^0, which is about fifteen per cent higher than the predicted value. Conservative predictions are a general quality of the first fracture approach, though the degree of conservatism in the estimated fracture strength of the laminate may be much greater than that found in this particular case.

A more accurate method of predicting the fracture strength of a multi-component specially orthotropic laminate is based on the use of strain energy release rates. It is shown in [3] that G_L, the strain

energy release rate indicative of crack growth in the laminate, may be expressed as the sum of the strain energy release rates characteristic of crack growth in the angle-ply components, weighted by the relative thicknesses of those components. Thus, in the case of the multi-component experimental laminate

$$G_L = 0.25\ G_Q^0 + 0.50\ G_Q^{45} + 0.25\ G_Q^{90} \tag{81}$$

The necessary values of G_Q for the angle-ply components may be calculated by substituting the fracture strengths of these components into (60). The component fracture strengths may, in turn, be predicted by (79a-b) or determined experimentally. The experimental results given in chapter IV are used here to obtain the following values of G_Q:

α	G_Q, lb-in/in^2
$\pm 0°$	117.
$\pm 45°$	45.0
$\pm 90°$	0.943

The predicted value of G_L is found to be 52.0 lb-in/in^2, when the above values of G_Q are substituted into (81). For comparison, the value of G_Q obtained by substituting the experimentally determined fracture strength of the multi-component laminate into (60) is 55.1 lb-in/in^2. The agreement between G_L and G_Q for the multi-component experimental laminate suggests that the initiation of crack growth

in such laminates may be accurately predicted in terms of the characteristic strain energy release rates of the angle-ply components.

VI.5 Effects of material heterogeneity

The applicability of metals-based LEFM to fiber composite laminates is largely based on the validity of a homogeneous material model for such laminates. The validity of this model cannot be fully evaluated without significant amounts of additional test data. However, some preliminary conclusions may be drawn, based on the information presently available.

The validity of the homogeneous material model is investigated by considering the size of the region ahead of the crack that is characterized by the elastic stress singularity,

$$\sigma \sim K/\sqrt{2\pi r} \tag{82}$$

The region in which (82) is valid is, by definition, the crack-tip region. The size of this area, denoted by ℓ_0, may be estimated from the results of the Inglis problem [35], the isotropic analog of the mode I problem discussed in chapter II. The results of the Inglis problem are shown in Figure 26, as a plot of transverse stress ahead of the crack vs. distance from the crack tip. In this plot, it is seen that the stresses exhibit the singular behavior described by (82) over a region extending approximately 0.40a from the crack tip.

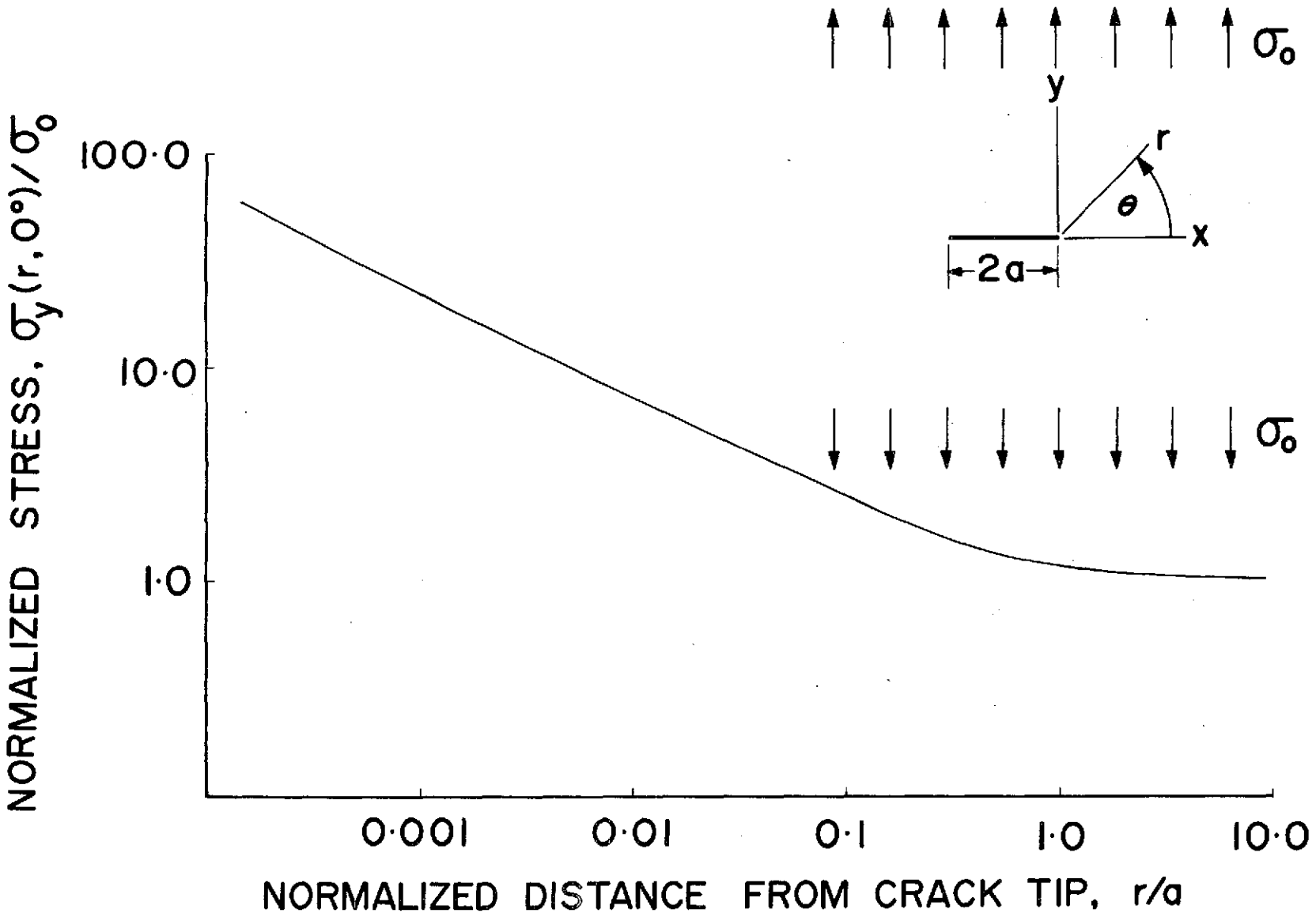

Figure 26. Results of the Inglis problem (insert). Plot of normalized transverse stress on the crack axis vs. normalized distance from the crack tip.

It is noted that this value of ℓ_o is probably an upper limit; a reasonable lower limit, estimated for the bend specimens discussed in chapter IV, is $\ell_o \geq 0.10$ a. Thus, for the smallest initial crack considered in the test program (a = 0.2 inch), $\ell_o \geq 0.02$ inch. For the graphite/epoxy material used in the test program, a crack-tip region of 0.02 inch contains at least fifty fibers per layer. The fact that the elastic stress singularity characterizes so many fibers would seem to justify the use of the homogeneous material model.

However, the elastic stress singularity does not characterize all of the fibers in the crack-tip region. As noted above, there exists some "zone of uncertainty", within which the material behaves inelastically. The size of this zone of uncertainty is r_f for a fiber-dominated material. For the graphite/epoxy material considered in the test program, it is shown above that $r_f = 0.0074$ inch. Thus, the elastic stress singularity characterizes only about thirty fibers per layer in the graphite/epoxy bend specimens having an initial notch size of 0.2 inch. Apparently, this is not a large enough number of fibers to justify the use of homogeneous material model, as the results obtained from the specimens having the smallest initial notch were somewhat spurious (see chapter IV). In order to ensure the validity of the homogeneous material model, and hence the LEFM approach in future tests of graphite/epoxy laminates, it is recommended that the initial crack size be chosen such that $\ell_o/r_f \geq 5$.

VI.6 Conclusions

The fracture strength of a single angle-ply laminate can apparently be predicted, using the principal elastic properties of the ply, the ply orientation, and the two principal fracture strengths of the ply. Moreover, the fracture strengths of single angle-ply laminates may be combined, as strain energy release rates, to characterize crack growth in a laminate having several angle-ply components. Clearly, both of these predictive methods require additional experimental verification.

The application of a homogeneous, metals-based LEFM model to cracked graphite/epoxy laminates seems to be justified, if the crack is sufficiently large. Again, the need for additional experimental data, particularly for other fiber/matrix material systems, is emphasized.

CHAPTER VII

CONCLUSIONS AND RECOMMENDATIONS

The results of this study indicate that the concepts and procedures of metals-based LEFM are to some degree applicable to the characterization of sharp notches in advanced fiber composites. It must, however, be recognized that this conclusion is based on a limited investigation of a very restricted class of problems and materials. As is the case in metals, there are surely instances in which the application of LEFM to fiber composite laminates is not warranted.

Some of the limitations of this work are rather obvious; for example, only mode I loading has been considered. Although some cases of mode II behavior were observed in the unidirectional 45° specimens, the effects of mode II and mode III (out-of-plane shear) loading of cracked composite laminates have yet to be investigated. Also, the work reported here is restricted to mid-plane symmetric laminates, which precludes any consideration of the stretching-bending coupling present in non-symmetric laminates. Such coupling would, of course, induce mode III crack behavior in response to mode I and/or mode II loading, adding a significant degree of complexity to the task of characterizing the initiation of unstable crack growth in a non-symmetric laminate.

The possibility that unstable growth of an existing crack is preceded by some amount of stable crack extension has also been ignored

in this work. However, this omission is not thought to be particularly serious for the laminates considered in this work, since P_Q, the load corresponding to initial unstable crack growth, is within ten per cent of P_{max}, the peak load, in all but the unidirectional 0° specimens. This finding implies that, with the exception of the 0° specimens, no significant changes in specimen compliance, e.g., stable crack growth, occurred prior to crack instability. Of course, this same result may not obtain in other laminates.

A more subtle constraint upon this work stems from the nature of the model of a composite laminate upon which this investigation is based. This model is based, in turn, upon the assumption that global strains are uniform through the thickness of the laminate. This assumption places certain limitations on the types of multi-directional laminates which can be modelled. In particular, the individual plies of a multi-directional laminate must be thin; thus, the deformation of any given ply is strongly constrained by the deformations of the adjacent plies in the laminate, on which it exerts an equally strong influence, in turn. Also, the thin ply restriction serves to prevent the occurrence of strain gradients through the thickness of a given ply. Moreover, the effects of a free edge appear to be active over a distance of approximately one ply thickness from the edge of a laminate [36]; the restriction of this work to thin-ply laminates is thus especially critical, since the region of interest in the fracture process is necessarily close to the

free edge at the crack tip. In fact, it may be that the minimum size of an effective crack is a function of ply thickness, rather than fiber diameter *per se*, as discussed in chapter VI.

As long as a laminate is constructed in a mid-plane symmetric fashion, using thin plies, the total thickness of the laminate seems to have little effect on the validity of an LEFM approach. The laminates tested by Halpin [29] and Weiss [30] were much thinner (on the order of 0.05 inch) than the laminates tested in this work. Nonetheless, the results obtained by these investigators are consistent with the results of this study (see chapter IV).

A final point of interest concerning the limits of this work is related to the effects of stacking sequence, i.e., the order in which the individual plies are arranged in the laminate. There is evidence that two laminates, made up of identical plies, may exhibit different modes of crack growth, depending upon the order in which those plies are arranged. In one case, the classical fracture mode observed in this investigation is obtained; in the other, a complex failure mode consisting of delamination and subsequent independent crack growth within the individual plies can occur. While the latter case is clearly a fracture process, it has no analog in homogeneous metals; thus, there is not obvious way of characterizing this complex failure mechanism using metals-based LEFM. However, there is some indication that this failure process may be avoided by choosing the stacking sequence to

induce compressive, rather than tensile stresses between plies near the crack tip [37].

The limitations of this study suggest some areas in which further work is necessary. In particular, the effects of non-symmetric loadings and stacking sequence must be investigated; the characterization of sharp notches in laminates which are not thin-plied and mid-plane symmetric is a matter of lesser importance, as most composites used for engineering applications are thin-plied and mid-plane symmetric.

Further studies of the anisotropic finite correction factor are warranted. The apparent material dependence of this parameter must be confirmed in specimen geometries and laminates other than those considered here; the accurate determination of the finite correction factor for composite bend specimens is particularly important. It is also necessary that the material dependence of the anisotropic finite correction factor be related to the elastic properties of a composite laminate; such a relation would permit the prediction of the anisotropic finite correction factor, thus obviating the need to calculate this parameter on a case-by-case basis.

Additional fracture test data for fiber composite laminates is also urgently needed. In particular, fracture data for specially orthotropic laminates having one or more single angle-ply components are needed to verify the predictive models discussed in chapter VI. In order to facilitate comparisons of fracture data, it is recommended

that future tests be performed in close agreement with the present standards for fracture testing of metals, if only for the sake of uniformity. The results discussed in this report indicate that the use of standard procedures for collecting and reducing test data is particularly important.

It is suggested that data be reported in the form of strain energy release rates, rather than fracture strengths. While these two parameters are related analytically, the energy concept does rest on a firmer physical foundation. Moreover, as was shown in chapter VI, the strain energy release rate provides a better means of predicting the behavior of complex laminates than does the fracture strength approach.

The significance of this work lies in the demonstrated applicability of a simple engineering approach to the study of fracture in advanced fiber composites. At least under some circumstances, it is seen that the notch sensitivity of a fiber composite may be characterized, using the well known approach of metals-based LEFM, in a way that is useful to the structural designer. Admittedly, LEFM is appropriate to only a limited class of composite problems, which has yet to be fully defined. Nonetheless, metals-based LEFM does appear to be a useful tool for the study of fracture phenomena in advanced fiber composite laminates.

REFERENCES

1. Waddoups, M. E., Eisenmann, J. R., and Kaminski, B. E., "Macroscopic Fracture Mechanics of Advanced Composite Materials", *Journal of Composite Materials* 5 (1971) 446-454.
2. *The Behavior of Advanced Filamentary Composite Plates with Cutouts*, Progress Report, Contract F33615-70-C-1308, Grumman Aerospace Corp., Bethpage, New York (1972).
3. Cruse, T. A., "Tensile Strength of Notched Composites", *Journal of Composite Materials* 7 (1973) 218-229.
4. Eisenmann, J. R., and Kaminski, B. E., "Fracture Control for Composite Structures", *Engineering Fracture Mechanics* 4 (1972) 907-913.
5. Zweben, C., *New Understanding of Fiber Composite Structures*, NASA Tech Brief 71-10161, Technology Utilization Office, National Aeronautics and Space Administration, Code KT, Washington, D. C. (1971).
6. Zweben, C., "On the Strength of Notched Composites", *Journal of the Mechanics and Physics of Solids* 19 (1971) 103-116.
7. Tetelman, A. S., "Fracture Processes in Fiber Composite Materials", in *Composite Materials: Testing and Design*, ASTM STP 460, American Society for Testing and Materials, Philadelphia, Pennsylvania (1969) 473-502.

8. Piggott, M. R., "Theoretical Estimation of Fracture Toughness of Fibrous Composites", *Journal of Materials Science* 5 (1970) 669-675.

9. Olster, R. F., and Jones, R. C., "Toughening Mechanisms in Continuous Filament Unidirectionally Reinforced Composites", in *Composite Materials: Testing and Design (Second Conference)*, ASTM STP 497, American Society for Testing and Materials, Philadelphia, Pennsylvania (1972) 189-205.

10. Thomason, P. F., "The Surface Energy of Fracture in Continuous-Fibre Metal-Matrix Composites", *Journal of the Mechanics and Physics of Solids* 20 (1972) 153-163.

11. Wu, E. M., "Fracture Mechanics of Anisotropic Plates", in *Composite Materials Workshop*, Technomic Publishing Co., Inc., Stamford, Connecticut (1968) 20-43.

12. Wu, E. M., "Application of Fracture Mechanics to Anisotropic Plates", *Journal of Applied Mechanics* 34 (1967) 967-975.

13. Hancock, J. R., and Swanson, G. D., "Toughness of Filamentary Boron/Aluminum Composites", in *Composite Materials: Testing and Design (Second Conference)*, ASTM STP 497, American Society for Testing and Materials, Philadelphia, Pennsylvania (1972) 299-310.

14. Zimmer, J. E., "Fracture Mechanics of a Fiber Composite", *Journal of Composite Materials* 6 (1972) 312-315.

15. Underwood, J. H., *Crack-Tip Deformation Measurements Accompanying Fracture in Fibrous and Laminar Composites*, Technical Report WVT-

7201, Benét Weapons Laboratory, Watervliet Arsenal, Watervliet, New York (1972).

16. Ashton, J. E., Halpin, J. C., and Petit, P. H., *Primer on Composite Materials: Analysis*, Technomic Publishing Co., Inc., Stamford, Connecticut (1969).

17. Lekhnitskii, S. G., *Theory of Elasticity of an Anisotropic Body*, Holden-Day Inc., San Francisco, California (1963).

18. Williams, M. L., "On the Stress Distribution at the Base of a Stationary Crack", *Journal of Applied Mechanics* 24 (1957) 109-114.

19. Srawley, J. E., and Brown, W. F., Jr., *Plane Strain Crack Toughness Testing of High Strength Metallic Materials*, ASTM STP 410, American Society for Testing and Materials, Philadelphia, Pennsylvania (1967).

20. Bowie, O. L., and Freese, C. E., "Central Crack in Plane Orthotropic Rectangular Sheet", *International Journal of Fracture Mechanics* 8 (1972) 49-58.

21. Cruse, T. A., and Swedlow, J. L., *Interactive Program for Analysis and Design Problems in Advanced Composites Technology*, AFML-TR-71-268, Air Force Materials Laboratory, Air Force Systems Command, Wright-Patterson Air Force Base, Ohio (1971) 160-273.

22. Chan, S. K., Tuba, I. S., and Wilson, W. K., "On the Finite Element Method in Linear Fracture Mechanics", *Engineering Fracture Mechanics* 2 (1970) 1-18.

23. Bowie, O. L., "Analysis of an Infinite Plate Containing Radial Cracks Originating from the Boundary of an Internal Circular Hole", *Journal of Mathematics and Physics* 35 (1956) 60-72.

24. Snyder, M. D., *Crack Tip Stress Intensity Factors in Finite Anisotropic Plates*, Doctoral Thesis, Department of Civil Engineering, Carnegie Institute of Technology, Carnegie-Mellon University, Pittsburgh, Pennsylvania (1973).

25. Tentative Method of Test E 399 for Plane-Strain Fracture Toughness of Metallic Materials, *1970 Annual Book of ASTM Standards*, Part 31, American Society for Testing and Materials, Philadelphia, Pennsylvania (1970) 911-928.

26. Paris, P. C., and Sih, G. C., "Stress Analysis of Cracks" in *Fracture Toughness Testing and Its Applications*, ASTM STP 381, American Society for Testing and Materials, Philadelphia, Pennsylvania (1964) 30-81.

27. Pinckney, R. L., and Freeman, R. B., *Determination of Physical and Structural Properties of Mixed-Modulus Composite Materials*, D210-10196-1, Eustis Directorate, U. S. Army Air Mobility Research and Development Laboratory, Fort Eustis, Virginia (1971).

28. Cruse, T. A., and Stout, M. G., "Fractographic Study of Graphite-Epoxy Laminated Fracture Specimens", *Journal of Composite Materials* 7 (1973) 272-276.

29. Halpin, J. C., U. S. Air Force Materials Laboratory, Wright-Patterson Air Force Base, Ohio, private communication, 1971.

30. Weiss, O. E., Convair Aerospace Division, General Dynamics Corporation, Fort Worth, Texas, private communication, 1971.

31. Griffith, A. A., "The Phenomena of Rupture and Flow in Solids", *Philosophical Transactions of the Royal Society (London)*, Series A, 221 (1921) 163-198.

32. Orowan, E., "Energy Criteria of Fracture", *Welding Research Supplement, The Welding Journal*, 34 (1955) 157-160.

33. Rice, J. R., "A Path-Independent Integral and the Approximate Analysis of Strain Concentrations by Notches and Cracks", *Journal of Applied Mechanics* 35 (1968) 379-386.

34. Hayes, D. J., *Some Applications of Elasto-Plastic Analysis to Fracture Mechanics*, Doctoral Thesis, Department of Mechanical Engineering, Imperial College of Science and Technology, University of London, London, England (1970).

35. Goodier, J. N., "Mathematical Theory of Equilibrium Cracks", in *Fracture*, volume 2, Academic Press, New York, New York (1968) 1-66.

36. Rybicki, E. F., and Hopper, A. T., *Analytical Investigation of Stress Concentrations due to Holes in Fiber Reinforced Plastic Laminated Plates, Three-Dimensional Models*, Battelle Columbus Laboratories, Columbus, Ohio (to appear).

37. Eisenmann, J. R., Convair Aerospace Division, General Dynamics Corporation, Fort Worth, Texas, private communication, 1973.